THESIS

DESIGN AND PERFORMANCE CHARACTERIZATION OF A SOLID-FUEL RAMJET GROUND-TESTING FACILITY

Submitted by
Riley Zane Duffens
Department of Mechanical Engineering

In partial fulfillment of the requirements
For the Degree of Master of Science
Colorado State University
Fort Collins, Colorado
Spring 2026

Master's Committee:

Advisor: Ciprian Dumitrache

Bret Windom
Thomas Bradley

ABSTRACT

DESIGN AND PERFORMANCE CHARACTERIZATION OF A SOLID-FUEL RAMJET GROUND-TESTING FACILITY

Renewed interest in high-speed air-breathing propulsion for sustained supersonic flight has intensified the need for experimental characterization of solid fuel ramjet (SFRJ) combustor flowfields, ignition processes, and flame stabilization mechanisms. Despite decades of analytical and numerical study, experimental data for SFRJ configurations remain sparse due to the limited availability of optically accessible, well-characterized test facilities. This work presents the design, fabrication, and preliminary baseline testing of a modular experimental SFRJ combustion facility. An existing indraft supersonic wind tunnel was reconfigured into an optically accessible testbed capable of both cold-flow and reacting-flow operation. The facility integrates high-speed schlieren imaging for time-resolved visualization of compressible flow structures, fast-response pressure transducers for combustor flow characterization, and a high-power continuous-wave laser ignition system (maximum output 330 W) for non-intrusive, remote ignition of solid fuel grains. The test-section flowpath was sized using an in-house quasi-one-dimensional gas-dynamic model. A dual-nozzle configuration was adopted, consisting of an upstream accelerating nozzle that established a target Mach number of 0.5 in the combustion chamber and a downstream choking nozzle that fixed the facility mass flow rate and test duration. Detailed mass and energy balance (including solid fuel regression modeling) were used to dimension the grain bed and ensure consistent operation under both cold-flow and reacting conditions. Initial testing focused on facility validation and baseline characterization through cold-flow experiments and preliminary combustion trials. Static pressure measurements confirmed a Mach 0.54 flow within the combustion chamber, in agreement with the design model. Combustion experiments employed hydroxyl-terminated polybutadiene (HTPB) as the base polymeric binder. To enable reliable laser-initiated ignition and sustained flameholding in an air-breathing environment, the grains incorporated a controlled fraction of conventional rocket motor energetic material to introduce a localized oxidizer source within the surface layer. Fuel grains incorporating up to 51.2 wt% KNO_3 demonstrated repeatable laser-initiated ignition and the formation of a persistent recirculation zone downstream of a backward-facing cavity flameholder. Schlieren diagnostics revealed a reattaching shear layer within the cavity, consistent with cavity-stabilized flameholding behavior in high-speed combustors. Importantly, these formulations did not self-sustain combustion in quiescent atmospheric conditions, confirming that oxidizer availability remained air-limited and that sustained burning was achieved only within the high-speed recirculation environment. The results establish a validated, cost-effective experimental platform for future parametric studies of fuel regression rates, flame stability limits, and energetic additive effects, providing critical experimental insight to support the development and scaling of solid fuel ramjet propulsion systems.

TABLE OF CONTENTS

LIST OF TABLES

LIST OF FIGURES

Chapter 1

Introduction & State-of-the-art

1.1 Introduction to High-speed Air-breathing Propulsion

Advancements in high speed air breathing propulsion offer a vast array of benefits over traditional propulsion technologies. One such benefit is the use of incoming air as an oxidizer thus reducing the need to carry unnecessary weight onboard. This increases the efficiency of any propulsion source and provides many improvements to the vehicle. Such benefits consist of increased tactical range, increase Mach envelope, reduced cost per flight, and enable faster response time [2]. With the possibility to revolutionize both military and civilian flight, high speed air-breathing propulsion is very commonly considered as the next large step in aerospace propulsion.

Typically, aerospace propulsion can be broken down into two forms, air breathing and non-air breathing propulsion. Common forms of non-air breathing propulsion include traditional liquid and solid rocket propulsion. With either of these, the vehicle carries both fuel and oxidizer and produces thrust via a combustion reaction. A common metric for the efficiency of a propulsive device is the Specific Impulse (Isp). Simply put, the specific impulse is a measure of how efficiently a propulsive device uses its propellant. Shown in Figure 1.1 is a graph that details the relationship between Mach flight regime and Isp.

A key distinction between rocket propulsion and airbreathing propulsion lies in whether oxidizer is carried onboard or supplied by the environment. For conventional rockets, both fuel and oxidizer are carried as propellant, and the performance of the system can be expressed through the classical Tsiolkovsky rocket equation:

$$\Delta v = I_{sp}\, g_0 \ln\left(\frac{m_0}{m_f}\right), \tag{1.1}$$

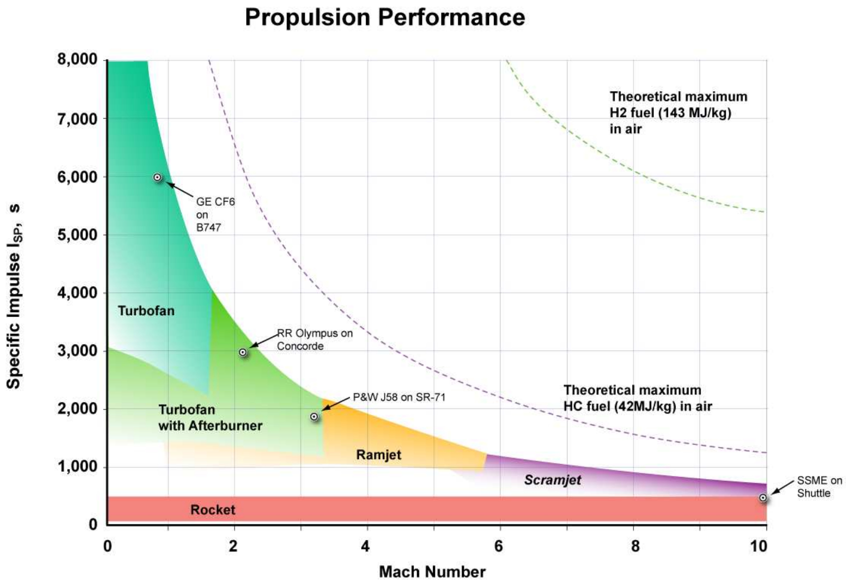

Figure 1.1: Specific impulse vs. Mach number for high-speed flight propulsion technologies [1].

where m_0 and m_f denote the initial and final mass of the vehicle, respectively, and I_{sp} and g_0 are the specific impulse and gravitational acceleration. The applicability of Eq. (1) rests on the assumption that the vehicle constitutes a closed system: the mass ejected through the nozzle is precisely the mass carried onboard as propellant.

Airbreathing engines, including turbojets, ramjets, scramjets, and solid-fuel ramjets, violate this assumption because they ingest oxidizer directly from the atmosphere. Consequently, airbreathing systems are not closed, and their performance cannot be evaluated using the rocket equation in its classical form. In particular, the system expels considerably more mass than it carries onboard as propellant.

To enable meaningful comparison between rockets and airbreathers, it is convenient to introduce an effective specific impulse defined with respect to onboard propellant only

$$I_{sp,\text{eff}} \equiv \frac{F}{\dot{m}_{\text{onboard}} g_0}, \tag{1.2}$$

where F is thrust and $\dot{m}_{\text{onboard}}$ represents the rate at which onboard fuel and oxidizer are expended. For a conventional rocket, all propellant is carried onboard, and the total reactive mass equals the onboard propellant mass. Therefore,

$$I_{sp,\text{eff},\text{RKT}} = I_{sp,\text{RKT}} = \frac{v_e}{g_0}, \tag{1.3}$$

where v_e is the effective exhaust velocity.

For an air breathing engine (AB), the situation differs. Let m_f denote the fuel mass and m_{ox} the total oxidizer mass required by stoichiometry. Let $\chi \in [0, 1]$ denote the fraction of that oxidizer carried onboard. The remaining fraction $(1 - \chi)m_{ox}$ is supplied by the atmosphere. Thus

$$m_{\text{onboard},\text{AB}} = m_f + \chi m_{ox}, \tag{1.4}$$

$$m_{\text{tot}} = m_f + m_{ox}. \tag{1.5}$$

Assuming, for simplicity, that the thermochemical exhaust velocity v_e is approximately the same for the two systems, the effective specific impulse of the AB becomes

$$I_{sp,\text{eff},\text{AB}} = \frac{m_f + m_{ox}}{m_f + \chi m_{ox}} \, I_{sp,\text{RKT}}. \tag{1.6}$$

Define the onboard reactive mass fraction,

$$\xi(\chi) \equiv \frac{m_f + \chi m_{ox}}{m_f + m_{ox}}, \tag{1.7}$$

so that

$$I_{sp,\text{eff},\text{AB}} = \frac{1}{\xi(\chi)} \, I_{sp,\text{RKT}}. \tag{1.8}$$

Because $m_{ox} > 0$ for any chemically meaningful propellant mixture and $0 \leq \chi \leq 1$, it follows that $\xi(\chi) \leq 1$, with equality only for $\chi = 1$. Therefore,

$$I_{sp,\text{eff},\text{AB}} \geq I_{sp,\text{RKT}}, \tag{1.9}$$

and

$$I_{sp,\text{eff},\text{AB}} > I_{sp,\text{RKT}} \quad \text{whenever} \quad \chi < 1. \tag{1.10}$$

This result establishes that using external air for the fuel oxidation process yields the maximum performance benefit, in good agreement with Figure 1.1. However, at high mach numbers additional aerodynamic and thermochemical constraints limit the performance of pure air-breather engines such as gas turbines and ramjets/scramjets.

An interesting compromise is the solid-fueled ramjet (SFRJ) engine which combines the cycle of a solid-fueled rocket engine with that of a ramjet. Since SFRJs typically operate with $\chi \ll 1$ (i.e., with fuel-rich grains that rely on atmospheric oxygen for combustion), their effective specific impulse exceeds that of an equivalent rocket burning the same fuel–oxidizer mixture. From a system perspective, this improvement in effective specific impulse translates into higher payload fraction, increased range, and reduced onboard propellant burden thus motivating the interest in better characterizing these systems.

1.2 Introduction to Ramjets

Ramjets represent a simple and efficient class of air-breathing propulsion devices specifically tailored for high-speed flight Mach number (typically, Ma 3.0-5.0), within the flight envelope of a typical rocket engine. These propulsive devices have been explored within three main categories: liquid fueled ramjets (LFRJ), solid fueled ramjets (SFRJ), and integral rocket ramjets (IRR) [12]. LFRJ work by injecting a liquid fuel into the combustor where it mixes and burns with incoming air. Similar to liquid rocket engines, this type of ramjet offers more precise control of the combustion process and greater flexibility during flight but requires complex injection and atomization systems.

SFRJs, by contrast, rely on the pyrolysis of a solid fuel grain lining the combustor wall. This system offers greater simplicity over the LFRJ but at the cost of more challenging mixing and flame holding dynamics. IRR's employ a dual-purpose combustor that serves initially as the solid fuel rocket combustion chamber during the boost phase. Once the fuel grain is consumed, the inlet air is allowed to enter the combustor where it encounters either a liquid fuel spray or a secondary fuel grain (starved in oxidizer). As such IRR's can be thought of as a hybrid between a ramjet and a rocket engine and can be operated either in liquid or solid fuel configuration [2]. A general schematic to all three configurations can be found in Figure 1.2.

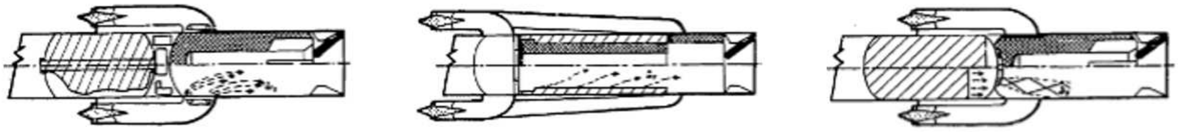

Figure 1.2: Schematics of; Liquid Fueled Ramjet (left), Solid Fueled Ramjet (Center), Integral Rocket Ramjet (Right), [2]

While significant attention has historically been given to traditional LFRJ technology, SFRJs remain comparatively underrepresented in both commercial development and the current propulsion market [12]. Despite this, SFRJs have generated renewed interest due to their potential to combine the simplicity and rapid response characteristics of solid rocket systems with the efficiency benefits of air-breathing propulsion. Retrofitting existing military ordnance and solid-fuel rocket platforms with air-breathing technology offers a compelling pathway to significantly extend operational range while preserving fast ignition and throttle-free operation. Beyond military applications, SFRJs also present opportunities for augmenting mid-supersonic flight in long-range civilian applications, where improved efficiency and reduced onboard oxidizer mass are desirable. Their relatively simple mechanical design, coupled with the absence of complex fuel injection and pumping systems, makes SFRJs attractive candidates for robust, low-maintenance propulsion solutions in regimes where conventional turbojet or rocket systems are less effective.

A SFRJ utilizes a solid fuel grain as the primary propellant source, with combustion initiated and stabilized by an anchored flame at the head of the combustor. This flame acts as a continuous ignition source, sustaining a diffusion flame along the length of the fuel grain as oxidized flow passes through the combustion chamber. The resulting high-temperature combustion products are then expanded through a converging–diverging nozzle to generate thrust. A schematic representation of a typical SFRJ configuration is shown in Figure 1.3. The simplicity of this configuration belies the complex coupling between flowfield dynamics, flame stabilization, and fuel regression that ultimately governs SFRJ performance and stability [2].

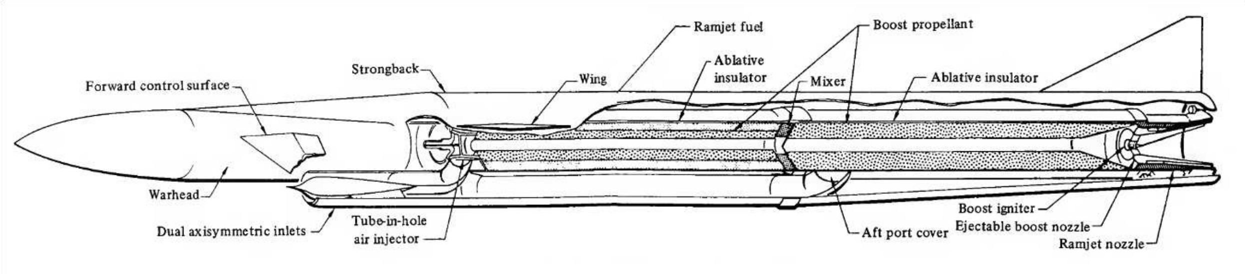

Figure 1.3: SFRJ Schematic From [2]

Improvements in SFRJ technology have traditionally focused on two primary areas of research, fuel grain chemistry and flameholding technology. Advances in fuel grain chemical formulation aim to optimize combustion efficiency by tailoring the binder, oxidizer content, and additive composition, thereby reducing reliance on embedded oxidizer and more effectively leveraging the air-breathing nature of SFRJ propulsion. Improvements in flameholding technology focus on stabilizing combustion across a wider range of operating conditions. Effective flameholding is critical for extending blow-off limits and maintaining a stable anchored flame under varying flow velocities, pressures, and thermal environments. Enhancements in flameholder design and flow control directly expand the operational envelope of SFRJ engines and improve robustness during ignition and sustained operation. Together, these two areas, fuel formulation and flameholding form the foundation of ongoing SFRJ research.

1.2.1 SFRJ Fuel Chemistry

Like traditional fuels used in solid rocket engines, SFRJ fuels are typically fuel-rich composite mixtures in which an oxidizer source is suspended within a polymeric binder. This formulation approach is well established, providing predictable burning behavior and mature manufacturing methods. Common binder materials include hydroxyl-terminated polybutadiene (HTPB), poly(methyl methacrylate) (PMMA), and polyethylene, among others [13]. These binder materials serve as both the structural matrix of the fuel grain and as the energetic fuel component during combustion. Within the binder matrix, oxidizer sources and additional additives are homogeneously suspended to tailor the overall burning characteristics of the fuel grain. Common oxidizers include ammonium perchlorate (AP), potassium nitrate (KNO_3), and sulfur-based compounds [14]. In addition to oxidizers, metallic additives are frequently incorporated to control regression rate and combustion behavior. Metals such as aluminum and magnesium are commonly used due to their high combustion energies and their influence on burning characteristics [15–17]. Adjusting the binder composition, oxidizer loading, or additive content can therefore have significant effects on the final burning behavior of the fuel grain.

An example of a typical AP-loaded composite fuel grain is shown in Figure 1.4. Common HTPB-based fuel grain formulations utilizing AP as an oxidizer may contain as much as 75% AP by weight. This high oxidizer loading highlights the critical importance of fuel grain formulation and its direct impact on combustion and regression characteristics in SFRJ systems.

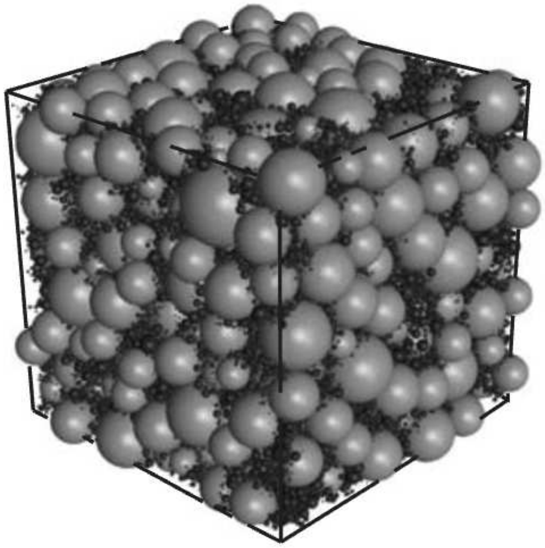

Figure 1.4: Typical packing of ammonium perchlorate bolstered fuel grain, from [3]

In an idealized configuration, the reliance on embedded oxidizer within the fuel grain could be significantly reduced for Solid Fuel Ramjet systems. As SFRJ are air-breathing propulsion devices that ingest atmospheric oxygen during operation, a portion of the oxidizer demand is supplied directly by the freestream air. This fundamental distinction motivates the pursuit of fuel grain formulations with reduced internal oxidizer loading, shifting a greater fraction of the combustion process to depend on atmospheric oxygen. Realizing this idealized behavior in practice is no so straight forward as combustion stability, ignition reliability, and regression behavior remain strongly coupled to fuel grain formulation. Understanding these limitations and the degree to which oxidizer content can be reduced while maintaining robust combustion provides a key motivation for continued experimental investigation of SFRJ fuel grains and their interaction with the combustor flowfield.

1.2.2 SFRJ Flameholding

A backward-facing cavity step is commonly employed to promote flameholding in ramjet and solid fuel ramjet (SFRJ) combustors. This is accomplished by generating a recirculation zone that enhances gas-phase mixing and stabilizes the flame near the forward section of the combustor. The sudden geometric expansion at the step induces boundary layer separation, forming a low-velocity recirculating region that can anchor combustion products and provide a continuous ignition source for incoming reactants. As understanding and characterization of this flameholding mechanism have improved, backward-facing steps have been extensively explored in both liquid fuel ramjet (LFRJ) and SFRJ applications [18].

Previous studies have focused on achieving finer control of the boundary layer and characterizing key flow features associated with the recirculation region, including reattachment length, reattachment location, and unsteady reattachment behavior such as flapping [4, 10]. These features play a critical role in determining flame stability, mixing efficiency, and overall combustor performance. In addition to backward-facing steps, flameholders may also take the form of recessed cavities. Cavity-based flameholders further extend blow-off limits by providing a protected region in which hot products and radicals can be retained, allowing stable combustion to persist across a wider range of operating and flight conditions. Schematic representations of both backward-facing step and cavity flameholder geometries are shown in Figure 1.5.

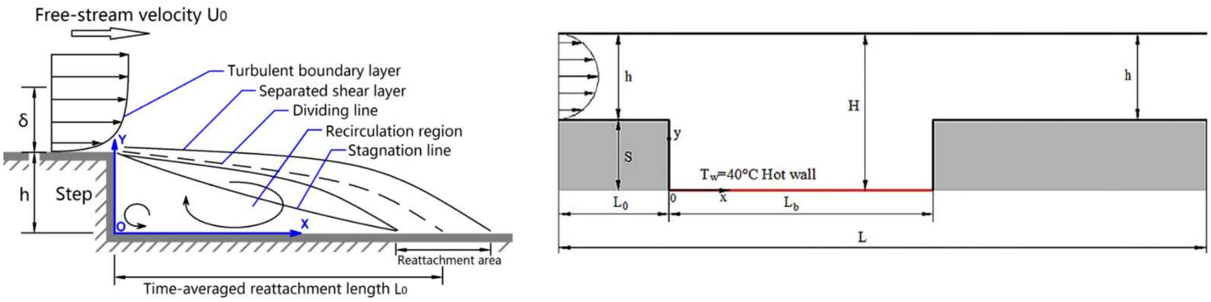

Figure 1.5: Schematics of backward Facing Step (Left) [4] and Cavity (Right) [5] Flame holders

In the case of a backward-facing step geometry, combustion products generated within the flameholding recirculation zone propagate downstream. This provides both radiative and convective heating to the remaining fuel grain and creates a distributed diffusion flame. This configuration results in two distinct combustion regions separated by the collapse of the shear layer, the recirculation zone immediately downstream of the step and the redeveloping boundary layer zone farther downstream. A schematic illustrating these regions is shown in Figure 1.6.The sharp velocity gradient across the separating shear layer makes this region particularly susceptible to combustion-driven instabilities. These instabilities can manifest as oscillatory motion or flapping of the shear layer, which is subsequently convected downstream and can disrupt the overall combustion process [4,19]. The severity of these instabilities can vary widely, ranging from low-amplitude, barely perceptible fluctuations to large-scale disturbances that result in flame blowout or complete unstart of the engine. Characterization of this shear layer flutter and its coupling with the combustion process is therefore essential to advancing the understanding and design of stable SFRJ combustors.

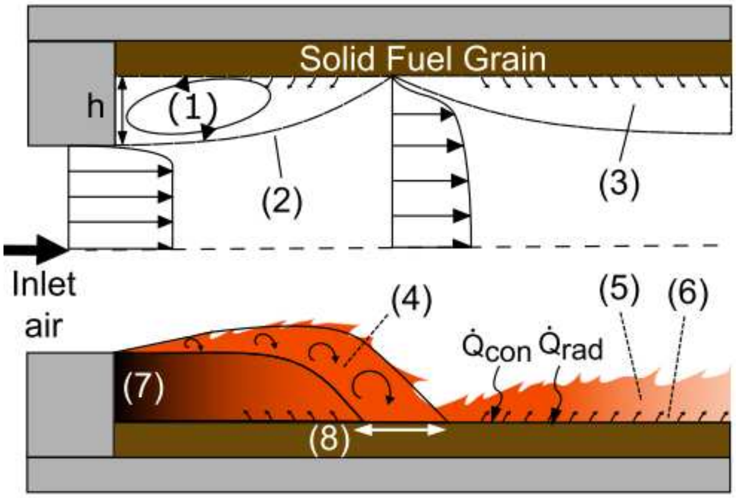

Figure 1.6: Cavity Flameholder From [6]

1.3 Review of Wind Tunnels

1.3.1 Purpose and Scope of Experimental Facilities

Wind tunnels provide a cost-effective and experimentally accessible means of studying both internal and external flow phenomena across a wide range of flow regimes [7, 20, 21]. While wind tunnels are most commonly associated with the visualization and characterization of external aerodynamic flowfields, their utility extends well beyond this traditional application. In particular, wind tunnels play a critical role in the investigation of internal flows, including both reacting and non-reacting systems [22, 23], where controlled boundary conditions and repeatable operating environments are essential.

Within this broader category, there exists a relatively underexplored subset of wind tunnel experimentation focused on flows within internal cavities, such as the combustion chambers of air-breathing propulsion systems. These internal flows are characterized by strong coupling between turbulence, mixing, heat release [24, 25], and condensed-phase fuel regression [26, 27]. The experimental investigation of such environments presents unique challenges, including limited optical access, short flow residence times, and sensitivity to upstream boundary conditions [11, 23]. These challenges have motivated the development of specialized experimental facilities designed to isolate and characterize internal reacting flows under propulsion-relevant conditions.

1.3.2 Classification of Experimental Facilities

Experimental facilities used in the study of high speed air breathing propulsion can be broadly characterized based on the presence of chemical reactions [23, 24]. This distinction provides a useful framework for organizing experimental approaches. The following subsections outline the defining characteristics, capabilities, and limitations of non-reacting and reacting flow facilities as they relate to propulsion-relevant research.

Non Reacting Flow Facilities

Non-reacting flow facilities, commonly referred to as cold-flow facilities, are designed to investigate fluid mechanical phenomena in the absence of chemical reactions. These facilities are widely used to characterize baseline aerodynamic behavior, including flow uniformity, shock structure, boundary-layer development, and turbulence characteristics, under controlled and repeatable conditions. By excluding heat release, cold-flow experiments enable isolation of key gas-dynamic parameters such as Mach number, Reynolds number, and pressure gradients, facilitating the application of similarity laws and scaling analyses [7, 20, 28].

Cold-flow facilities are particularly valuable during early stages of facility development and experimental planning, where validation of inlet flow quality, nozzle performance, and test-section uniformity is required prior to the introduction of combustion. However, the absence of heat release and density variation limits their applicability to propulsion systems in which combustion-induced effects such as thermal choking, pressure rise, and flow–chemistry coupling play a dominant role. As a result, cold-flow facilities serve primarily as a foundational tool rather than a complete representation of reacting propulsion environments [23, 24].

Reacting Flow Facilities

Reacting flow facilities extend cold-flow experimental concepts by incorporating chemical reactions and heat release, thereby enabling investigation of combustion processes under controlled flow conditions. The presence of combustion introduces additional complexity through strong coupling between turbulence, mixing, chemical kinetics, and thermodynamic property variation. These effects significantly influence flow stability, pressure distribution, and overall facility behavior, particularly in confined internal geometries relevant to propulsion applications [24, 25].

Reacting flow facilities encompass a broad range of experimental configurations, including combustion wind tunnels, direct-connect rigs, impulse facilities, and open or semi-confined combustion setups. Compared to non-reacting facilities, reacting flow experiments face increased challenges related to thermal management, flow residence time, facility-induced choking, and diagnostic access. Despite these challenges, reacting flow facilities are essential for capturing the physical processes governing flame stabilization, ignition, and combustion efficiency in air-breathing propulsion systems. Their development and operation therefore represent a critical step toward experimentally realistic simulation of propulsion-relevant internal flows [11, 23, 29].

1.3.3 Types of Wind Tunnel Experimentation Platforms

Closed-Loop Facilities

Closed-loop, fan-driven wind tunnels represent one of the earliest and most widely used experimental platforms in aerodynamic testing. In these facilities, the working fluid is continuously recirculated through the tunnel circuit, allowing precise control of flow conditions and efficient long-duration operation. Closed-loop tunnel concepts have been employed in aerospace research since the earliest days of aeronautical experimentation, with systematic development dating to the late nineteenth century, and they remain common for low-speed and low–Mach-number investigations today [7, 30, 31].

Closed-loop facilities are particularly well suited for low–Mach-number testing under conditions representative of low-altitude flight. Their ability to operate continuously with stable flow conditions makes them attractive for large-scale experiments, and many such facilities feature test sections with cross-sectional dimensions on the order of several meters. These characteristics enable high-quality measurements of aerodynamic forces, flow uniformity, and large-scale flow structures. While closed-loop tunnels are most commonly associated with low-speed testing, a limited number of closed-circuit facilities capable of supersonic operation have also been developed [32–34]. A schematic view of a representative closed-circuit wind tunnel configuration is shown in Figure 1.7.

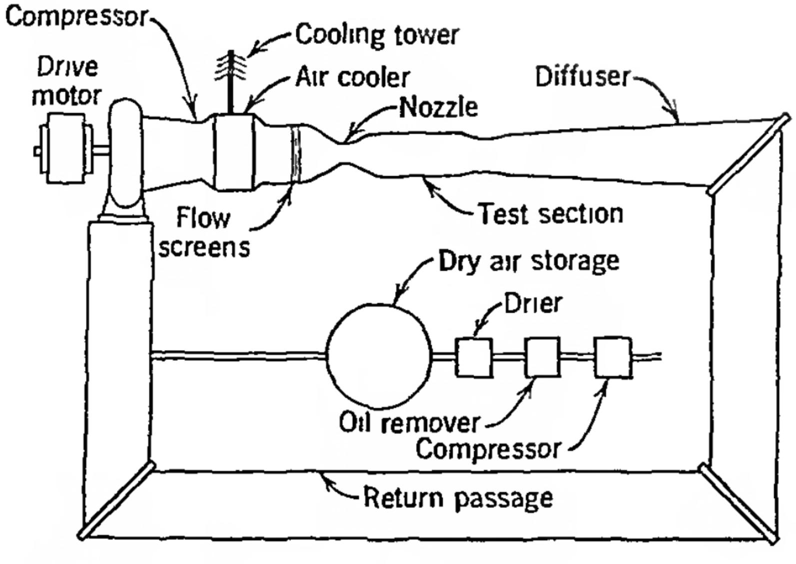

Figure 1.7: Closed Circuit facility overview, From [7]

Despite these advantages, closed-loop wind tunnels are generally ill suited for continuous combustion testing. Because the working fluid is recycled within the system, sustained combustion can lead to progressive depletion of oxygen and accumulation of combustion products in the incoming flow, resulting in altered thermochemical conditions and reduced experimental repeatability. For this reason, closed-loop facilities are typically limited to non-reacting flow studies or short-duration combustion experiments where gas composition changes are negligible.

Blow Down Facilities

Blow-down wind tunnel facilities are characterized by the use of a finite reservoir of high-pressure gas that is expanded through the test section during operation. In contrast to closed-loop facilities, blow-down tunnels operate in an open-circuit configuration, with the working fluid exhausted to the atmosphere or a downstream dump volume. This mode of operation enables access to significantly higher pressures, Mach numbers, and a greater range of flight conditions than are typically achievable in fan-driven facilities, making blow-down tunnels well suited for high-speed aerodynamic and combustion research [7,28]. In Figure 1.8 a schematic of a Blowdown facility can be seen.

Blow-down facilities are widely used across a broad range of flow regimes, from subsonic to hypersonic conditions. Many established facilities at government-led research institutions, including NASA and Arnold Engineering Development Complex, employ blow-down configurations to achieve the stagnation pressures and Mach numbers required for high-speed testing [35–40]. In addition to national laboratories, a large number of university-scale experimental facilities utilize blow-down tunnels to support research in compressible aerodynamics and high-speed reacting flows [41–48]. Depending on reservoir size and operating conditions, blow-down facilities provide test durations ranging from several seconds to several minutes, enabling quasi-steady measurements of both reacting and non-reacting flows. Because fresh air is supplied from the reservoir for each run, blow-down tunnels are generally more amenable to combustion experiments than closed-loop facilities, as oxygen depletion and accumulation of combustion products in the incoming flow are avoided. These characteristics make blow-down configurations a common choice for combustion wind tunnel testing across a wide range of operating conditions.

Despite these advantages, blow-down tunnels introduce limitations associated with finite test duration and unsteady reservoir depletion. During a run, stagnation pressure and temperature may vary unless actively regulated, which can complicate data interpretation and experimental repeatability. Additionally, the high mass flow rates and elevated pressures involved in blow-down operation impose increased structural, thermal, and safety requirements on facility hardware. As a result, blow-down facilities represent a trade-off between achievable operating conditions and experimental duration, and their design must balance propulsion relevance against controllability and operational complexity.

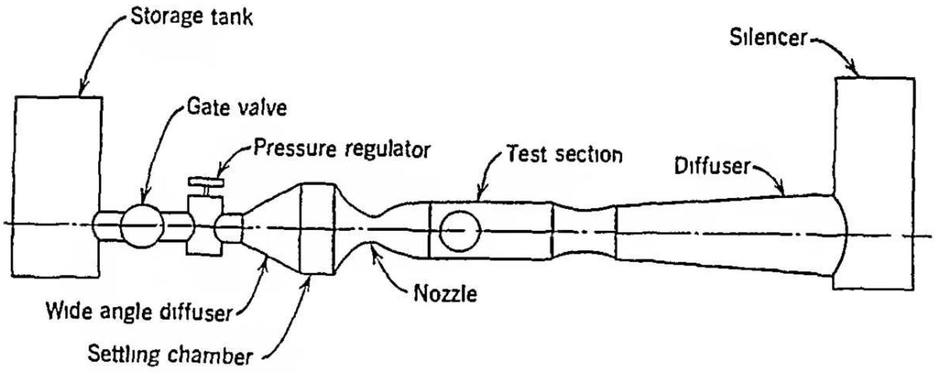

Figure 1.8: Blowdown facility overview, From [7]

Indraft Facilities

Indraft wind tunnel facilities operate by drawing ambient air through the test section using a downstream vacuum system, exhaust fan, or evacuated reservoir. Most indraft facilities are operated in an open-circuit configuration, with the working fluid entering from the atmosphere and exiting through a dedicated exhaust system [49–51]. This mode of operation provides a simple and robust means of generating internal flows without the need for large-footprint, high-pressure storage volumes. Indraft facilities are commonly used for subsonic and low-supersonic flow experiments. Because fresh air is continuously supplied from the environment, indraft tunnels are well suited for experiments involving combustion, as oxygen depletion and accumulation of combustion products in the incoming flow are avoided. Their steady operation also makes them attractive for studies requiring repeatable boundary conditions and extensive diagnostic access. A schematic of a typical indraft facility layout is shown in Figure 1.9.

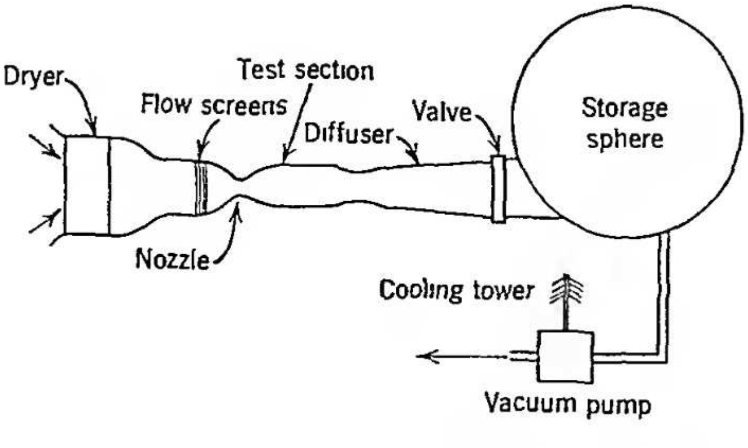

Figure 1.9: Indraft facility schematic, From [7]

Some facilities employ a combined blow-down–indraft configuration in which both vacuum potential and pressurized air are stored prior to a test [8, 40, 52]. While this form of indraft tunnel requires a larger facility footprint and higher capital cost, it offers increased flexibility and improved control over test-section flow conditions. A schematic of a representative combined blow-down–indraft facility is shown in Figure 1.10.

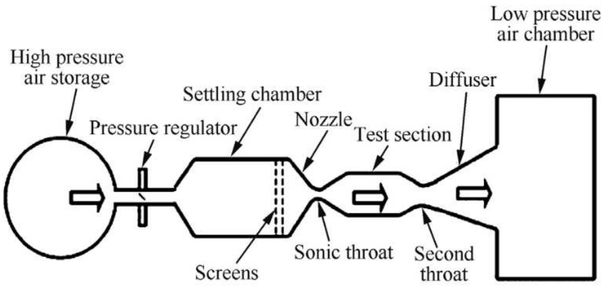

Figure 1.10: Schematic of a combined Blowdown-Indraft facility, from [8]

Despite these advantages, indraft facilities are generally limited in achievable stagnation pressure, stagnation temperature, and maximum Mach number by ambient conditions and exhaust system capacity. As a result, their application to high-speed propulsion research is constrained compared to blow-down or impulse facilities. Consequently, indraft tunnels are most often employed for low- to moderate-speed reacting-flow studies where experimental simplicity and repeatability are prioritized over extreme operating conditions.

1.3.4 Wind Tunnel–Based Combustion Facilities

Wind tunnel based combustion facilities encompass a wide range of experimental configurations designed to investigate reacting flows under controlled boundary conditions. While such facilities may be classified by operating Mach number or tunnel architecture, an equally important distinction arises from the form of fuel employed in combustion experiments. In high-speed propulsion research, experimental studies commonly involve either gaseous or liquid fuels, which emphasize injection, mixing, and ignition processes, or solid fuels, which introduce additional complexity through condensed-phase regression and fuel–surface interactions.

In contrast to liquid-fueled combustion experiments where fuel delivery and mixing dominate experimental design, solid-fuel combustion studies must account for coupled aerodynamic, thermal, and chemical processes occurring at a reacting fuel surface. These differences impose unique requirements on facility configuration, test duration, and diagnostic access. As a result, experimental platforms developed for solid-fuel and condensed-phase combustion represent a distinct subset of wind tunnel–based facilities and are discussed below.

Solid Fuel Ramjet Experimental Platforms

A variety of experimental platforms have been developed to investigate solid and condensed phase combustion within SFRJ's. These facilities are designed to study flame holding, fuel regression, and gas–solid interaction under conditions intended to approximate air-breathing propulsion environments.

One representative example is the experimental solid fuel ramjet facility developed at the Israel Institute of Technology, shown schematically in Figure 1.11. In this configuration, a high-pressure, high-temperature oxidizing flow composed of oxygen and nitrogen is injected over the solid fuel grain to drive combustion and regression, enabling controlled investigation of fuel grain burning rate and thrust behavior [9,53,54]. This approach has provided valuable insight into fuel regression mechanisms and overall combustion stability under well-defined operating conditions. However, because the combustor is fully enclosed and lacks optical access, detailed spatial characterization of flame structure and regression-zone dynamics remains limited.

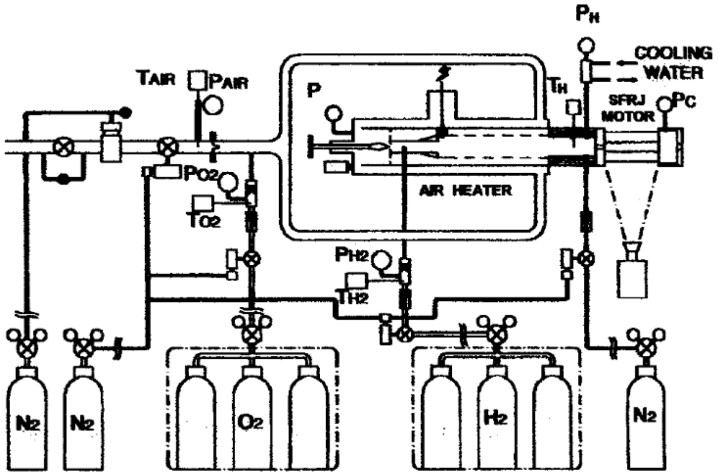

Figure 1.11: Israel Institute of Technology experimental facility elaborated scheme [9]

Another example of a solid fuel ramjet experimental platform is the direct-connect SFRJ facility developed by TNO, used to investigate sustained combustion limits of a central-dump combustor under simulated high-altitude flight conditions [10]. In this configuration, vitiated, heated air with controlled total temperature, mass flow rate, and pressure is supplied directly to the combustor, reproducing the thermodynamic conditions associated with Mach 2.5–3 flight at altitudes near 10 km. This allows for precise control over inlet air composition. Unlike fully enclosed rocket-stand configurations, this facility allows for partial optical access at lower combustor pressures, permitting visual identification of combustion modes including flame-out, partially sustained combustion, and fully sustained operation. This direct-connect approach provides a well-controlled environment for validating flame-holding models and studying regression-rate behavior. This facility is shown in Figure 1.12.

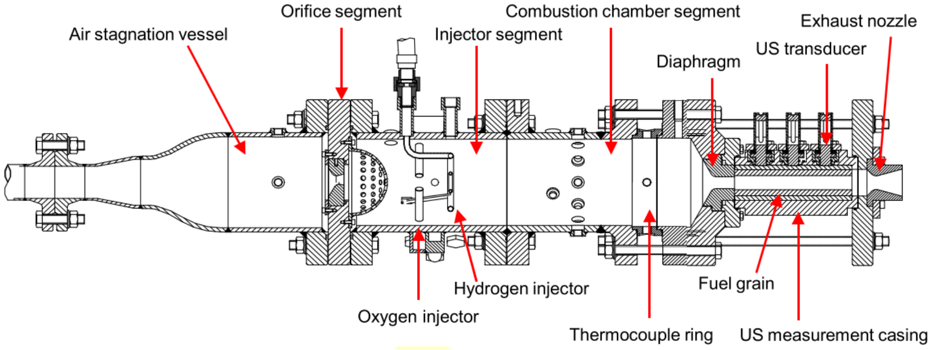

Figure 1.12: TNO SFRJ experimental platform [10]

A different approach to the study of SFRJ combustion behavior focuses on detailed characterization of flameholding zones within the combustor, where unsteady flow structures play a critical role in stabilizing combustion at high flow velocities. Researchers at Purdue University have developed a robust, optically accessible SFRJ combustor specifically designed to enable time-resolved diagnostics of the internal flowfield and flame stabilization mechanisms [6, 19, 55, 56]. This experimental platform incorporates a backward-facing step flameholder geometry, which is representative of common recirculation-based flameholding strategies used in air-breathing propulsion systems.

In this facility, particle image velocimetry (PIV) was employed in conjunction with spectral proper orthogonal decomposition (SPOD) to identify dominant unsteady flow structures and characteristic frequency modes associated with the flameholding process [55]. These diagnostics enable direct observation of coherent vortical structures within the recirculation zone and their interaction with the reacting flow, providing insight into the coupling between dynamic instabilities and combustion dynamics. The experimental configuration utilizes particle seeding and a pulsed Nd:YAG laser to resolve phase-averaged and time-resolved velocity fields, allowing quantitative analysis of flow unsteadiness that would be inaccessible in enclosed or non-optically accessible SFRJ platforms.

The optically accessible nature of the Purdue facility represents a significant departure from rocket-stand-based SFRJ experiments, which typically prioritize integral measurements such as thrust and regression rate but provide limited information on internal flow structure. By enabling spatially resolved, time-resolved measurements within the combustor, this platform allows for direct investigation of flameholding physics, including the role of shear-layer dynamics, recirculation strength, and dominant instability modes. As such, the Purdue SFRJ facility illustrates the advantages of wind tunnel–style airflow-driven experiments for advancing fundamental understanding of solid fuel ramjet combustion beyond bulk performance metrics alone. The experimental layout of this facility is shown in Figure 1.13.

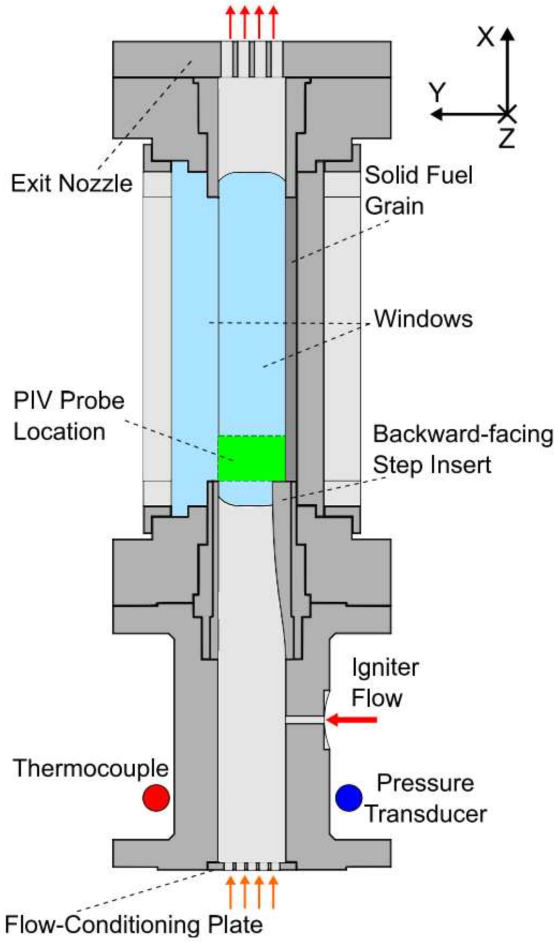

Figure 1.13: Purdue Experimental SFRJ Facility schematic [6]

1.3.5 Summary and Facility Comparison

The experimental facilities discussed in the preceding sections represent a range of approaches developed to investigate reacting flows and solid fuel ramjet combustion under controlled conditions. While this review is not exhaustive, the selected examples highlight the key trade-offs inherent in experimental propulsion research, including operating Mach number, test duration, airflow realism, diagnostic accessibility, and the ability to accommodate condensed-phase fuel regression. No single facility simultaneously satisfies all of these requirements, and experimental platforms are typically designed to prioritize a subset of relevant physical processes.

To facilitate comparison across these diverse experimental approaches, Table 1.1 summarizes representative wind tunnel–based combustion and solid fuel ramjet facilities reported in the literature. The table includes key parameters such as facility type, operating regime, oxidizer source, test duration, diagnostic capability, and primary research focus. This comparison provides a concise framework for evaluating existing experimental capabilities and identifying gaps that motivate the development of new experimental platforms.

Table 1.1: Comparison of representative solid fuel ramjet (SFRJ) experimental facilities

Facility / Reference	**Facility Type**	**Flow Source**	**Inlet Temperature**	**Inlet Pressure**	**Test Duration**	**Optical Access**	**Primary Research Focus**
Israel Institute of Technology SFRJ [9, 53, 54]	Rocket-stand SFRJ	High-pressure O_2/N_2	562–1200 K	345–1600 kPa	Steady / Long duration	None	Fuel regression and thrust performance
TNO Direct-Connect SFRJ [10]	Direct-connect SFRJ	Vitiated heated air	500–1500 K	460–990 kPa	Seconds–Minutes	Limited	Flameholding limits and extinction behavior
Purdue SFRJ [6, 19, 55, 56]	Blow-down tunnel	Vitiated heated air	655 K	460–685 kPa	Seconds	Excellent	Flameholding dynamics and unsteady mode analysis
North Carolina State University [57]	Blow-down tunnel	Electrically heated air	1000 K	1379 kPa	Seconds–Minutes	Excellent	Inlet characterization and fuel regression
Virginia Tech [58, 59]	Blow-down tunnel	Electrically heated air	923–1173 K	1300 kPa	Seconds	Excellent	Instability characterization and cavity design
Nanjing University [60]	Connected-pipe	Not reported	540 K	780 kPa	Seconds–Minutes	None	Numerical model validation and swirling study
DLR Germany [61]	Connected-pipe	Vitiated heated air	288–873 K	Not reported	Seconds–Minutes	None	Combustion stability and area ratio limits

The facilities summarized in Table 1.1 collectively demonstrate significant progress in ground-based solid fuel ramjet experimentation, yet several gaps remain that limit comprehensive understanding of SFRJ combustion physics. Most notably, facilities with excellent optical access for detailed flowfield diagnostics such as the Purdue, North Carolina State, and Virginia Tech blow-down tunnels—are constrained by test durations on the order of seconds, which may be insufficient to capture quasi-steady fuel regression behavior and long-timescale coupling between grain geometry evolution and combustion dynamics. In addition, facilities capable of extended test durations, such as the Israel Institute of Technology rocket-stand and TNO direct-connect configurations, offer limited or no optical access, precluding high-resolution measurements of flameholding mechanisms, turbulence-chemistry interactions, and instantaneous flowfield structure. Additionally, while several facilities achieve realistic inlet conditions, the simultaneous achievement of a near continuous run time, high pressure, and comprehensive optical diagnostic facility has not been demonstrated in a single platform. The present work addresses these limitations through the development of a new combination indraft / blow-down facility that combines extended test duration (targeting 60 seconds) and full test section optical access, enabling time-resolved characterization of both transient ignition phenomena and quasi-steady regression-coupled combustion over timescales relevant to fuel grain evolution.

Chapter 2

Facility Development

2.1 Facility Overview

In 2023 work began at Colorado State University on a state of the art supersonic wind tunnel facility. The Colorado State University APDL wind tunnel is an indraft wind tunnel that utilizes a 3.5 m^3 vacuum dump tank to sustain supersonic flow conditions within the test chamber via air suction directly from the atmosphere. A detailed description of the facility design and validation experiments are provided in Teeter et al. [50] and a figure of the original flow channel is shown in Figure 2.1 below. Steady flow within the test section is maintained as long as the pressure differential between the atmosphere and dump tank is large enough to maintain a choked nozzle flow. The dump tank is evacuated down to 5 millibar prior to each test to ensure maximum test duration. The inlet section includes three honeycomb flow straighteners to ensure laminar flow prior to fluid acceleration. The converging- diverging nozzle is designed using a custom-made method of characteristics code developed by APDL that is specifically tailored to provide flow free of expansion waves at the desired test section Mach number. The test section is defined by two parallel plates which are adjustable in height for a maximum cross-sectional dimension of 5.25" x 5.25". Mounting of test articles within the wind tunnel utilizes $\frac{1}{4}$-20" threaded holes spaced on a 1" grid drawing inspiration from industry standard optical tables. This modular design allows for the APDL team to quickly and accurately change the flow conditions within the wind tunnel from Mach 2.0-7.5. Actuation of the wind tunnel is automated with a pneumatic piston-driven rack and pinion system mounted to the 6-inch ball valve aft of the test section. This custom designed pneumatic actuator allows for fast actuation of the valve (down to 30 ms). Coupled with a data acquisition system and automated control, total test times are on the order of 20 minutes.

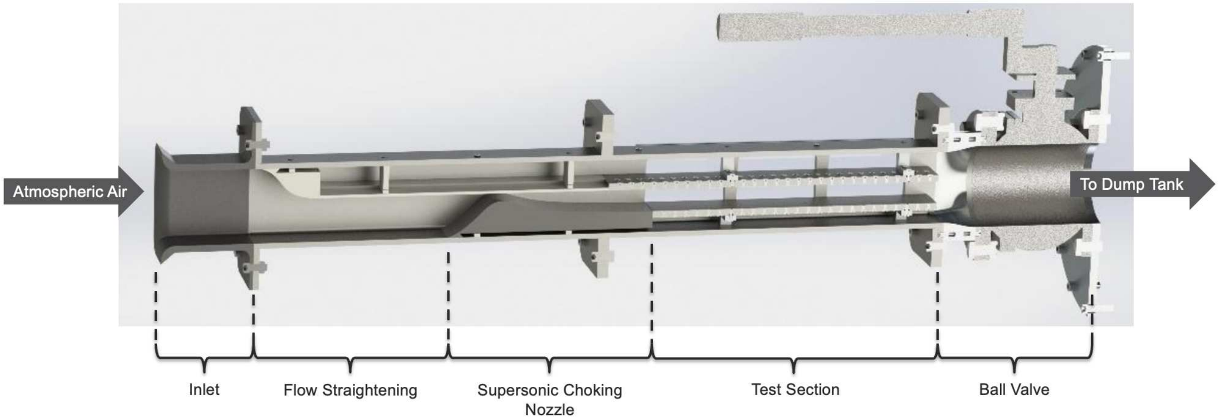

Figure 2.1: APDL Supersonic Tunnel Section View

To facilitate testing of SFRJ combustion, the tunnel platform was retrofit with new modules. As shown in Figure 2.2, the optically accessible combustion chamber was situated between two converging nozzles. The larger converging nozzle downstream of the test section is used to choke the system flow, maintaining a Mach number of 1 at the throat throughout the test. By fixing the mass flow rate throughout the test section with the downstream nozzle, a secondary nozzle can be designed to fix the combustion chamber inlet Mach number. This is accomplished by the upstream smaller converging nozzle. Finally integrated within the inlet nozzle assembly is also the fuel grain tray and the backwards step stabilization cavity. If a range of inlet Mach numbers are desired, the nozzle-fuel grain tray assembly can simply be replaced with a new one. This ground-up design of the new tunnel was created to allow for total control of both the gas dynamic design and mechanical fabrication of the new system.

This chapter has been split into two main sections. These are the gas-dynamic design, and the mechanical design and assembly of the tunnel. The gas-dynamic section will discuss a novel quasi 1-D code that was used to parametrically size the tunnel dimensions. The mechanical design section will discuss the manufacturing and final assembly of the tunnel.

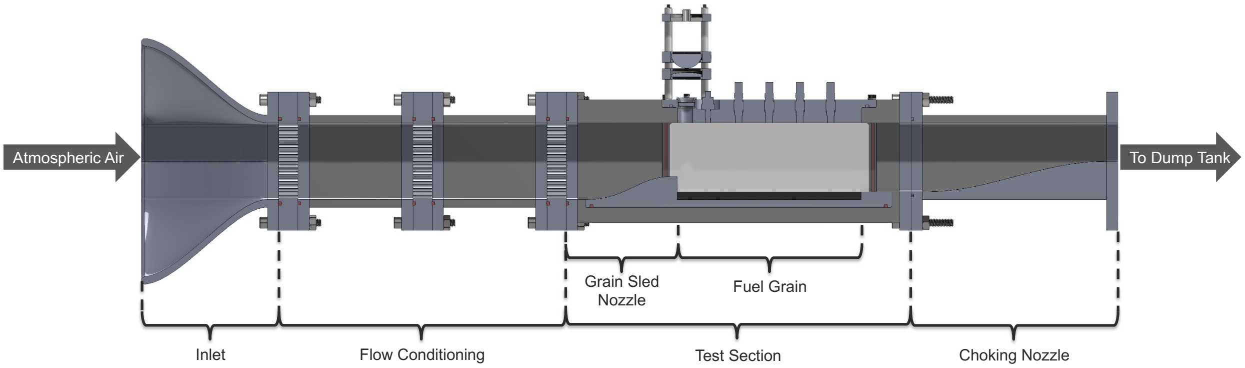

Figure 2.2: APDL SFRJ Tunnel Overview

2.2 Gas-dynamic Design

A 1-D isentropic flow simulation of the flow channel geometry was created in order to size the tunnel's nozzles, step height and fuel grain tray dimensions. From a gas dynamics point of view, the tunnel can be broken down into three main sections, as shown in Figure 2.3.

① Inlet and flow conditioning section, where the fluid is brought within the facility and the flow is condition back to laminar

② Combustor inlet, which is marked by the throat of the inlet converging nozzle

③ Fuel grain slab region, where a secondary mass flowrate is generated by the pyrolysis and combustion of the fuel grain

④ post-cavity combustor exit region

⑤ choking nozzle section where the total mass flowrate allowed through the wind tunnel is established

These planes represent changing flow conditions from the inlet of the tunnel to the dump tank. To correctly size the choking nozzle and the backward facing step the following equations outline the process for solving for determining the theoretical flow conditions at each area of interest.

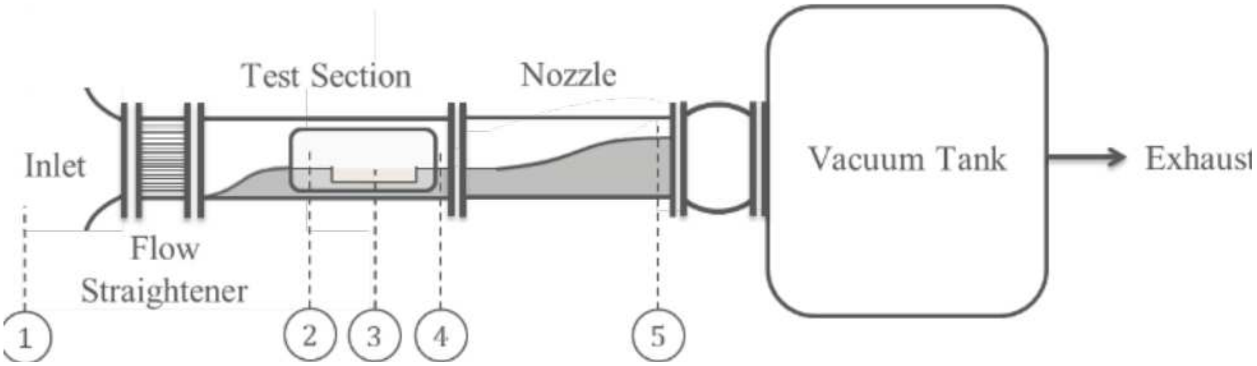

Figure 2.3: SFRJ Tunnel Schematic

The total mass flow rate of the combined air through the choking nozzle can be derived from conservation of mass. The subscripts represent the flow conditions at that subscript points in Figure 2.3, and can be written as:

$$(\dot{m}_{\text{total}})_5 = (\dot{m}_{\text{air}})_2 + (\dot{m}_{\text{grain}})_3 \tag{2.1}$$

The choking condition is established at point 5 through a normal shockwave at the throat. The properties of this choke point can be related to the total mass flow rate through the system using the isentropic flow relation for a choking nozzle. This is represented in Equation 2.2. Where γ is the ratio of specific heats, A_5 is the area at the choke point, P_2 is the static pressure before the choking nozzle, and T_{TS} is the post combustion gas temperature. The code was integrated with a chemical equilibrium solver to determine the correct flow conditions at every point within the quasi-1D flow-field (γ, T_{TS}, R_{g_4}).

$$(\dot{m}_{\text{total}})_5 = \frac{A_5 P_2}{\sqrt{(T_{TS})_4}} \cdot \sqrt{\frac{\gamma_4}{(R_g)_4}} \cdot \left(\frac{\gamma_4 + 1}{2}\right)^{-\frac{\gamma_4+1}{2(\gamma_4-1)}} \tag{2.2}$$

The mass flow rate of the fuel grain combustion can be estimated by using tabulated grain regression rates (ρ_{HTPB}, a, G_0^n) and the design dimensions (L_{grain}, W_{grain}) of the grain slab within the tunnel can be set as free parameters during the design phase. This assumes that during the duration of the test the grain is burning evenly, omitting a transient region of time for the flame front to propagate across the grain surface from ignition. The burn rate used for this calculation assumed a pure HTPB formulation and the fit parameters were taken from Evans et al. [62]. This relation is shown in Equation 2.3.

$$(\dot{m}_{\text{grain}})_3 = (\rho_{HTPB}) \cdot a \cdot G_0^n \cdot (L_{\text{grain}}) \cdot (W_{\text{grain}}) \tag{2.3}$$

Primary air addition into the system through the combustor inlet is first compressed from the nominal tunnel height at point 2 via the first converging nozzle. This design constraint lets the user control Mach number entering the grain cavity. The coupled equation that needs to be used for optimization is then obtained by plugging Equations 2.2 & 2.3 back into Equation 2.1. This is shown in Equation 2.4.

$$\frac{A_5 P_2}{\sqrt{(T_{TS})_4}} \cdot \sqrt{\frac{\gamma_4}{(R_g)_4}} \cdot \left(\frac{\gamma_4 + 1}{2}\right)^{-\frac{\gamma_4+1}{2(\gamma_4-1)}} = \rho_2 \cdot Ma_2 \cdot a \cdot A_2 + (\rho_{HTPB}) \cdot a \cdot G_0^n \cdot (L_{\text{grain}}) \cdot (W_{\text{grain}}) \tag{2.4}$$

Starting with equation 2.4, a parametric study with respect to grain dimensions and nozzle heights was performed to optimize the tunnel for a given combustor inlet design mach. The design Mach number for point 2 was Ma 0.45. This is comparable to other ramjet engines and test facilities [58]. The final dimensions for the tunnel free stream flow were computed to have a width of 2.5” with a height of 2.25”. The combustor inlet throat height and choking nozzle height were calculated to be 1.75” and 1.25” respectively. A stable runtime was estimated to be 3.06s and was calculated based on the vacuum tank pressure which will un-choke the outlet converging nozzle. The stable runtime can be calculated from continuity shown in Equation 2.5. Where V is the 3.5m^3 dump tank volume, P_{end} is the dump tank pressure at which the tunnel starts to unstart. $(\dot{m})_5$ is calculated with Equation 2.2.

$$t = \frac{P_{end} V}{(\dot{m})_5 (R_g)_4 (T_{TS})_4} \tag{2.5}$$

To calculate the pressure at which the tunnel starts to unstart (P_{end}) a relation can be derived to express when a shockwave appears inside of the nozzle. This relation is shown in Equation 2.6. Here the total pressure loss over the shock wave is represented as ($\frac{p_{02}}{p_{01}}$), the ratio of exit static to stagnation pressures ($\frac{p_e}{p_{0e}}$), and static pressure in the test section (p_{01}).

$$P_{end} = \frac{p_{02}}{p_{01}} \frac{p_e}{p_{0e}} p_{01} \tag{2.6}$$

The pressure loss over the shock wave ($\frac{p_{02}}{p_{01}}$) can be calculated as a function of upstream mach number (Ma_1). And is expressed in Equation 2.7.

$$\frac{p_{02}}{p_{01}} = \left(\frac{(\gamma+1)Ma_1^2}{(\gamma-1)Ma_1^2+2}\right)^{\frac{\gamma}{\gamma-1}} \left(\frac{\gamma+1}{2\gamma Ma_1^2-(\gamma-1)}\right)^{\frac{1}{\gamma-1}} \tag{2.7}$$

The ratio of exit pressures ($\frac{p_e}{p_{0e}}$) is calculated in Equation 2.8.

$$\frac{p_e}{p_{oe}} = \left(1+\frac{(\gamma-1)Ma_1^2}{2}\right)^{-\frac{\gamma}{\gamma-1}} \tag{2.8}$$

By varying each of the choking nozzle dimensions a heat map centered around Ma 0.4 can be generated for a chosen fuel grain dimension. This heatmap of test section mach numbers is shown in Figure 2.4.

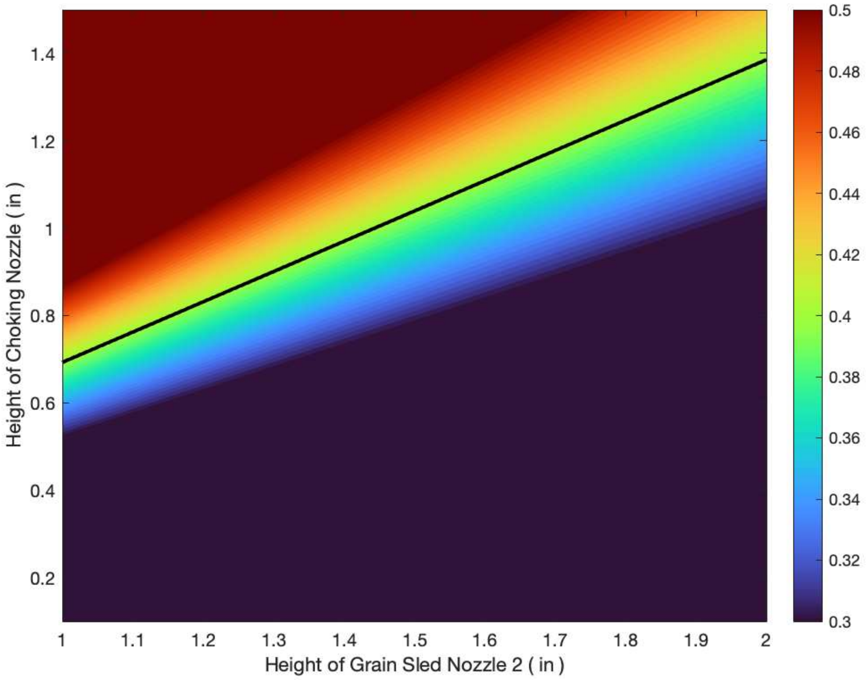

Figure 2.4: Heatmap of test section Mach numbers, black line represents Ma 0.4

2.3 Mechanical Design

2.3.1 Inlet and Flow Straightening

The inlet to the tunnel is open to the atmosphere and can be considered to draw from an infinite pressure far field. The geometry was designed for ease of additive manufacturing and takes the shape of a traditional bell intake plenum. Polylactic acid (PLA) was used for its low cost and ability to be re-manufactured in case of prototyping changes. Figure 2.5 shows the CAD design for the inlet geometry in addition to a machined flow straightener.

Figure 2.5: Tunnel inlet geometry (Left) and flow straightener plate after manufacturing (Right)

Conditioning of the flow prior to the test section is performed by three parallel plates. Many designs exist to create a uniform flow that mitigates both lateral velocity and transient vibrations. The most common of these are honeycomb or circular cells. For ease of manufacturing a lattice of circular precision drilled perforations was chosen. This design features a length to diameter ratio of L/d 8 for the cells. This was found to be within the optimal range for cancellation of lateral velocity and to reduce the turbulence within the flow field while limiting undesirable pressure drop over the straightening sections [21, 63]. As this section incorporates a modular design where all straightening sections can be interchanged, this design supports any future improvements. Two of the three flow straightening plates were machined from aluminum to protect against combustion heating, while the third was 3D printed from PLA filament.

2.3.2 Grain Sled and Flameholding Geometry

Backward Facing Step

The removable grain sled shown in Figure 2.6 incorporates the fuel grain attachment point in addition to the cavity step. Having this geometry self-integrated ensures that the fuel grain ignition spot remains the same during a variety of tests. It also ensures constant test conditions while being able to efficiently change fuel sources. The grain sled seals the tunnel with the use of an o-ring face seal on the bottom of the sled. The converging nozzle was created using a spline curve, to smoothly transition the laminar flow from the flow straightening section to the test section. This gradually increases the Mach number of the flow while maintaining the laminar flow created in the previous section. Researchers have extensively studied the flow behavior of non-reacting backward-facing steps, leading to advancements in understanding shear layer growth, reattachment characteristics, and vortex structures with their associated modes of instability. An experimental investigation by Ma et al. examined the flapping motion of a turbulent reattaching shear layer downstream of a two-dimensional backward-facing step. Velocity vector fields showed that the reattaching shear layer flaps vertically by approximately one step height, from the middle of the recirculation region to the reattachment area [4]. This motion results from oscillatory vortex impingement on the wall, influencing the degree to which fluid is re-injected toward the step compared to flow entrainment into the shear layer. When it moves upwards, the reattaching shear layer splits more to the reverse flow, leading to expansion of the recirculation region; when it moves downwards, the reattaching shear layer sharply impinges on the wall, leading to compression of the recirculation region. The time-averaged reattachment length varied from 5 to 8 step heights, depending on the incoming boundary layer state, turbulence intensity, and Reynolds number [4]. We have used this as a design criterion for sizing the step height of our cavity.

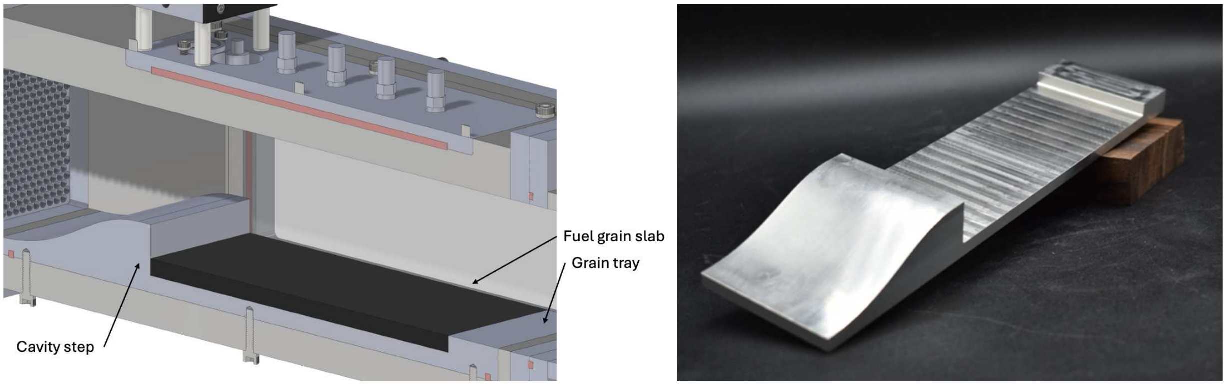

Figure 2.6: Fuel grain sled and backward facing step within assembly (left) and manufactured fuel grain sled (right)

Cavity Flameholding

In addition to the backward-facing step flameholder configuration, a cavity-based flameholding system was developed to investigate alternative stabilization mechanisms relevant to solid fuel ramjet combustion. Cavity flameholders have been extensively studied in supersonic and high-speed flow applications due to their ability to create stable recirculation zones that anchor combustion without the total pressure losses associated with bluff-body flameholders. The cavity geometry was designed based on established characterization studies of cavity length-to-depth (L/D) ratios and their influence on flow structure and flameholding performance [11]. As illustrated in Figure 2.7, cavity flow structures are typically classified into three distinct regimes based on the L/D ratio: open cavity flows, transitional flows, and closed cavity flows. In open cavity configurations (typically L/D < 10-13), the shear layer spanning the cavity opening exhibits periodic oscillations and impinges on the downstream cavity wall, creating a well-defined recirculation zone within the cavity. In closed cavity flows (typically L/D > 10-13), the shear layer reattaches to the cavity floor before reaching the downstream wall, resulting in a primary recirculation zone within the cavity and a secondary recirculation zone downstream. The transitional regime represents the intermediate behavior between these two limiting cases. For the present study, only open cavity flow regimes were investigated, as these configurations are more conducive to flameholding due to stronger coupling between the recirculation zone and the main flow.

The cavity flameholder hardware was designed to accommodate multiple L/D ratios through a modular blocking assembly, enabling systematic investigation of cavity geometry effects on flameholding and combustion stability. The initial design focused on L/D ratios of 1 and 6, representing the lower and upper bounds of the open cavity regime for the anticipated flow conditions. The complete cavity flameholder assembly is shown in Figure 2.8. The primary cavity block bolts directly onto the existing fuel grain sled using embedded 10-32 socket head cap screws, with precise alignment ensured through two 1/2-inch dowel pins that engage matching holes in the sled mounting interface. This dowel pin system prevents lateral or rotational misalignment during installation and ensures repeatable positioning across test runs. The baseline cavity depth was fixed

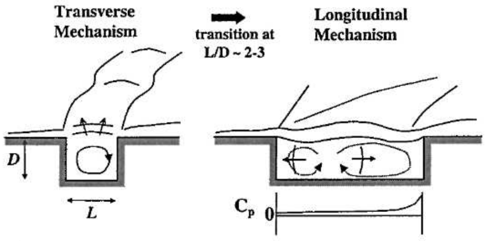

a) Open cavity flow for *L*/*D* < 7–10

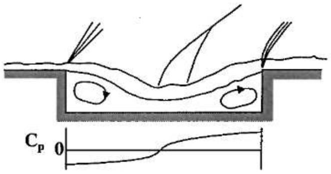

b) Closed cavity flow for *L*/*D* > 10–13

Figure 2.7: Cavity flow regimes as a function of length-to-depth ratio, showing open, transitional, and closed cavity configurations [11]

at 0.5 inches, yielding a maximum cavity length of 3 inches for the L/D = 6 configuration. To facilitate testing of intermediate L/D ratios without manufacturing multiple complete assemblies, a secondary blocking insert was designed to effectively shorten the cavity length. This insert can be either re-machined or adjusted to fit any desired future L/D between 1 and 6. This modular approach provides experimental flexibility while minimizing hardware costs and changeover time between test configurations. The cavity flameholder assembly integrates seamlessly with the existing optical access windows, allowing high-speed imaging and laser diagnostics to be applied to cavity flameholding studies without modification to the test section.

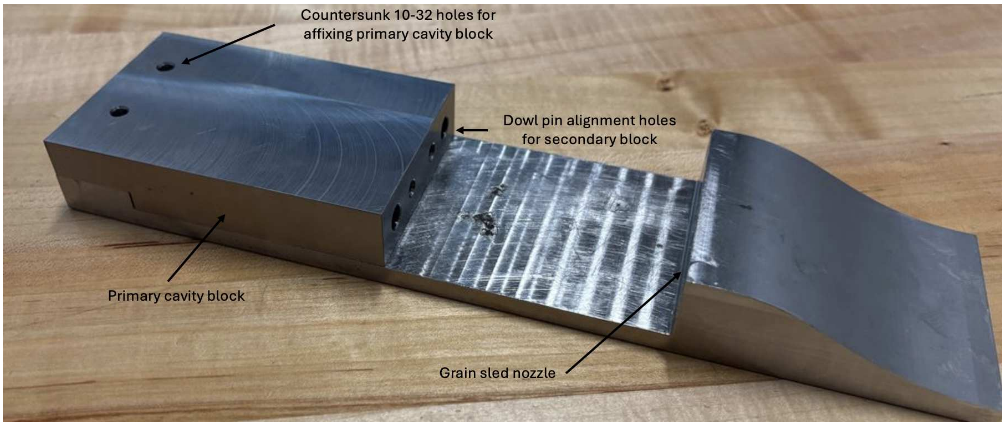

Figure 2.8: Modular cavity flameholder assembly showing grain sled with cavity block affixed

2.3.3 Test Section

The test section of the tunnel is comprised of the pressure transducer sled, laser ignition system, fuel grain tray, and optical window sub-assemblies. The housing was manufactured from sheets of 3/8” 304 stainless steel to resist extreme thermal expansion during tunnel operation. All sheets comprising the test section were then welded to form its final shape. The fuel grain tray slides out the front or back of the tunnel for flexibility of future improvements. 8-32 fasteners were used for all sub assembly attachment points where 1/4-20 bolts were used for tunnel section securement. Figure 2.9 shows the tunnel schematic in addition to the frame and sub components after preliminary manufacturing was completed.

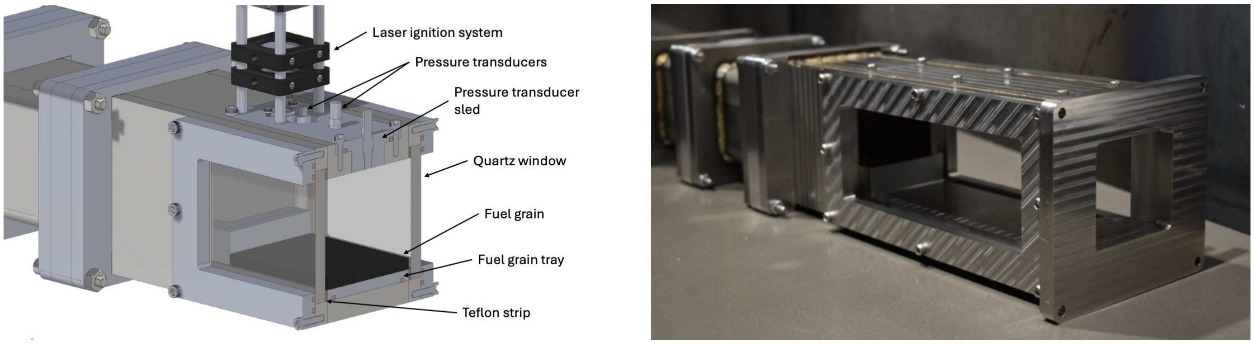

Figure 2.9: Test section cross section with component labels (left) and manufactured test section, before addition of laser ignition system and pressure transducer ports (right)

To protect against unnecessary stresses on the quartz windows, two strips of Teflon are placed in-between the window and stainless steel of the test section housing. Sealing of the windows is maintained through a dual o ring face seal on the outside of the tunnel. This helps to maintain constant pressure on each window for the duration of the test.

2.3.4 Choking Nozzle

Following the test section, a smaller throat section converging nozzle is used to limit the total mass flowrate in the tunnel (inlet air plus combustion products). The choking nozzle section was manufactured out of 304 stainless steel, welded directly at the bottom of the rectangular tube section. The design of the nozzle contour was created by an interpolated spline to smoothly compress the flow to the desired throat area. Initial testing was performed with 3D printed prototypes. This allowed the APDL staff to test various configurations of inlet Mach numbers and validate the gas dynamics code before manufacturing the final steel nozzle. Figure 2.10 shows the section view for the choking, and the manufactured nozzle contour prior to welding.

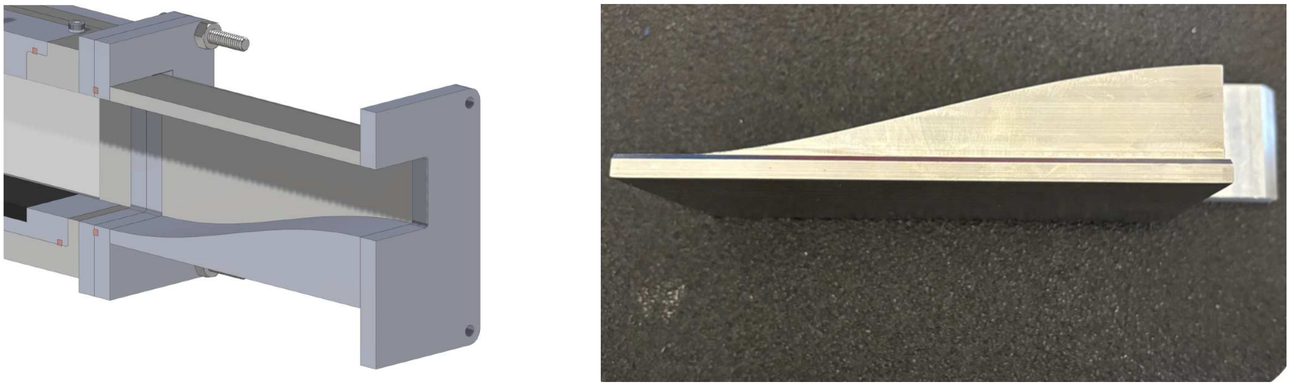

Figure 2.10: CAD image of choking nozzle section (left) and machined nozzle prior to welding (right)

2.3.5 Laser Ignition System

In order to ignite the fuel grain surface reliably and without perturbing the flow a laser ignition system was developed. Traditional ignition methods typically utilize an electric igniter embedded within the grain wall. For full flow systems that can safely eject the ignition source this typically works well. In the case of an experimental wind tunnel where accessing fuel grains would mean perturbing both the optical and flow path, a different solution is required. An adjustable 0-330 Watts CW fiber-coupled diode laser was utilized to direct energy into the fuel grain surface. This gives the user complete control of not only ignition timing, but initial ignition power as well. A study was conducted to estimate the amount of laser power required to heat the localized ignition point. A simple 0-D energy balance where the laser power addition is balanced by traditional loss mechanisms is given in equation 2.9.

$$0 = \eta \cdot \mathrm{P} - [\underbrace{\epsilon\sigma\mathrm{LW}\left(\mathrm{T}^4 - \mathrm{T}^4_{\text{ambient}}\right)}_{\text{Radiation}} + \underbrace{\frac{\mathrm{kLW}}{\mathrm{d}}\left(\mathrm{T} - \mathrm{T}_{\text{ambient}}\right)}_{\text{Conduction}} + \underbrace{\mathrm{hLW}\left(\mathrm{T} - \mathrm{T}_{\text{ambient}}\right)}_{\text{Convection}}] \tag{2.9}$$

The laser focal point is chosen to match the exposed surface of the grain. The laser spot size at the focus point is estimated using the equation for a real (non-ideal) Gaussian beam. This equation is shown in Equation 2.10, where a beam quality M2 = 5 was chosen (which is slightly overestimated to give a better representation of losses within the system). The focal length of the focusing Plano-convex lens f =100 mm and the wavelength of the CW laser λ = 976 nm. This results in an estimated laser focal area of 0.0283 mm. A relationship between laser input power and surface temperature and is shown in Figure 2.11. The plot shows that the 50 W to 100 W range is sufficient to support ignition of the HTPB slab and start the combustion process.

$$w_0 = \frac{4M^2\lambda f}{\pi D} \tag{2.10}$$

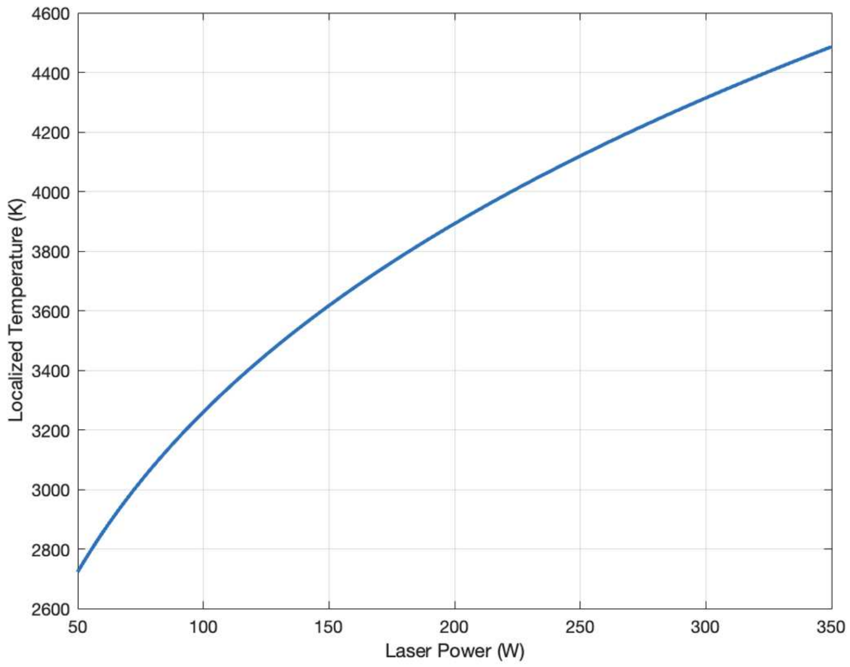

Figure 2.11: Laser power vs localized surface temperature

Experimentally, the laser power is delivered into the test section using an optical port embedded in the pressure transducer sled. A ½” sapphire optical window is placed between two rectangular cross-sectional sealing rings and compressed from the top via a retaining ring. Laser emission is delivered from a fiber optic at the top of the system. Light is collimated out of the fiber using a 25 mm plano-convex lens located at one focal length away from the fiber outlet. The collimated beam then focused on the surface of the fuel grain using a 100 mm plano-convex focusing lens. The system is built using a cage bracketing system which improves the rigidity of the system during operation but also allows fine tuning of the focusing point height in relation to the fuel grain (in some configurations it is beneficial to bury the laser focus up to 1 mm inside of the fuel grain). Measurement of the total transmission for the system resulted in an optical efficiency of 76%, which is reasonable for the hardware being used. The system is shown in Figure 2.12.

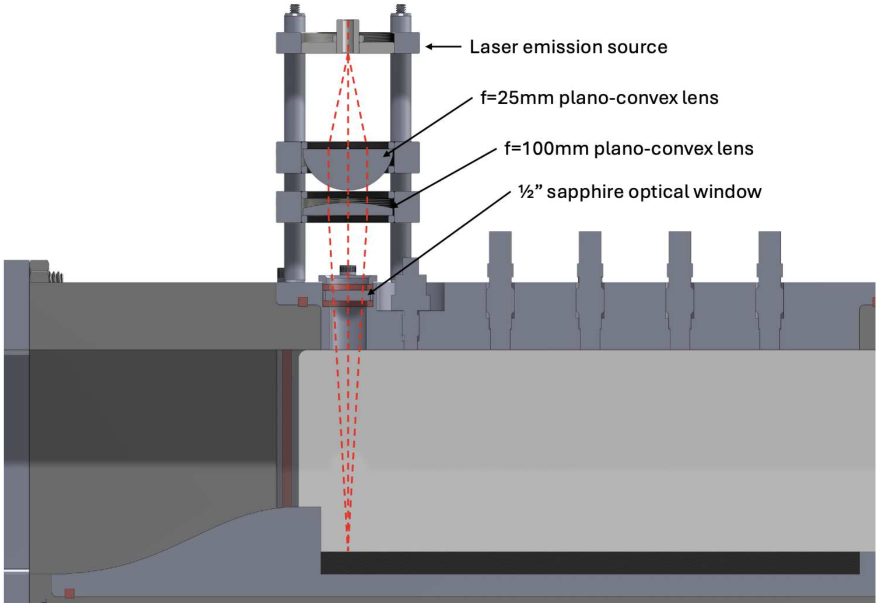

Figure 2.12: Laser ignition subsystem with component labels

2.4 Blow Down System Design and Commissioning

Through testing of the SFRJ tunnel the need for increased system reactivity became apparent. In practice there is two main ways to increase reactivity of the combustion process at a constant mach number. These are increasing the temperature of incoming air, and increasing the pressure of incoming air. Designs for a heated plenum air feed system had been previously created to facilitate higher air temperatures but were deemed to be not cost effective. The powerhouse energy campus where the APDL is located has a large supply of pressurized air stored in 6 ???? m^2 tanks that sit just outside of the APDL lab space. A piping system was designed and routed to deliver this air into the inlet of the SFRJ project. A Kimray AJL5 balanced pressure reducing regulator was chosen to better control testing pressures within the tunnel. Along with the pressure regulator, two grooved ball valves are used for control of the air flow. A schematic of this system is shown in Figure 2.13.

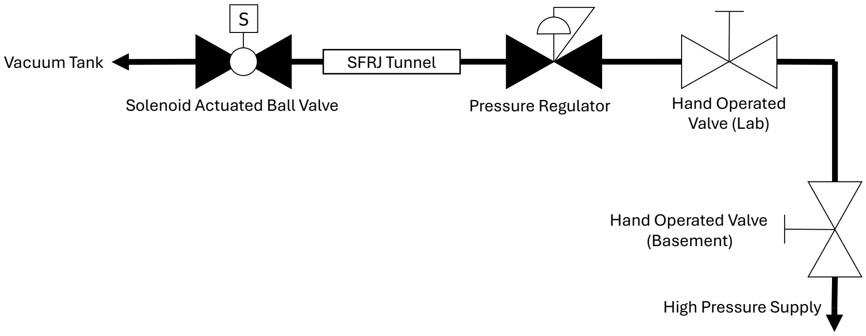

Figure 2.13: Schematic for blow-down air pressure system

Piping was routed through the basement of the powerhouse, out through the wall of the building, and back into the lab space through a window to preserve the natural aesthetics of the historic building and to hide the piping from general view. Once inside of the lab space the piping was routed to the floor to maintain walk-ability through the lab. Pictures of the lab space piping are shown in Figure 2.14, and a picture of the external piping is shown in Figure **??**. All piping was 3" schedule 40 iron piping and joined with groove locked connections. This created an easy system for assembly and to facilitate any future changes.

Figure 2.14: Lab space Blow down Piping

2.5 Flow Diagnostics – Schlieren & Pressure Transducers

To visualize high speed flow characteristics within the tunnel test section an optical diagnostic technique called schlieren imaging is utilized [**?**]. Light is collected from a light source by a plano-convex lens and focused down to a point source at the surface of an iris. The subsequent point source is then collected by an 8” parabolic mirror (f=800mm). A collimated beam is created from this mirror and passed through the test section. Any localized density gradients within the beam will change the index of refraction leading the collimated beam to refract as the exit the test section. The same process is repeated on the collection side of the system where the collector point source is created on a horizontal knife edge. Cutting the light at this point decreases the luminosity of the light source thereby improving image contrast. A CMOS camera is placed behind the knife edge to capture the image.

The primary emission spectra for combustion are centered at wavelengths in the red to infrared range. For this reason, a blue LED centered at 470 nm was chosen for the schlieren system. To further limit the spectra range that the CMOS camera detects, a GFP excitation filter which passes wavelengths 451-487nm and an IR blocking filter which passes wavelengths 375-650 nm are included in the system. These optical filters are centered next to the collector side knife edge. Figure 2.15 shows a top-down view of the tunnel along with the folded schlieren beam path. The emitter and collector sides of the schlieren system are shown on the right and left respectivly. To save space within the lab the schlieren system was folded two times which drastically reduces both the footprint of the system and vibrational effects on the system sensativity.

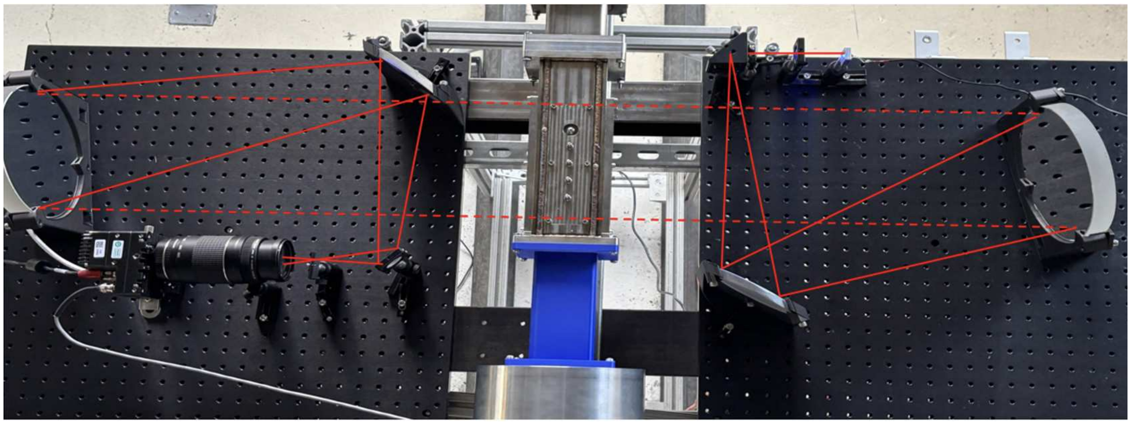

Figure 2.15: Folded Z schlieren diagnostics layout with beam path

The pressure transducer sled sits above the test section and provides a multifunctional platform that serves to both ignite the surface, and measure static and dynamic pressure within the tunnel. To measure static pressure within the test section a Kulite XTL-190 is embedded at the forward end of the sled. Following this, four PCB-113B28 dynamic pressure transducers are embedded equlodistantly along the pressure transducer sled. These high frequency pressure transducers have a working range of 100 kHz and serve to determine whether any combustion instabilities develop within the combustor. The locations of these pressure transducers within the tunnel are shown in Figure 2.16. All pressure transducers sit flush with the bottom of the sled to mitigate any helmholtz resonance typically seen in offset cavity transducers.

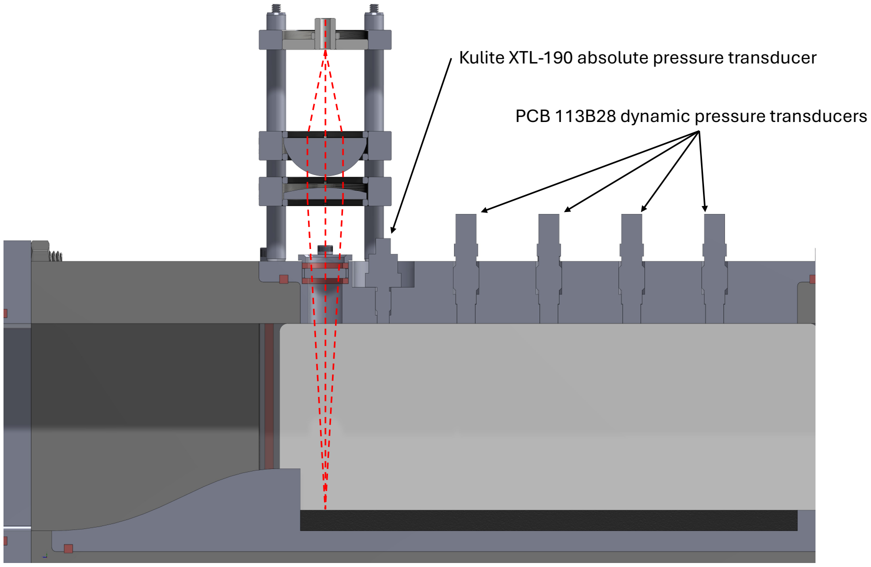

Figure 2.16: Pressure Transducer Layout

2.6 Facility Assembly

The final tunnel configuration mounts directly to the pneumatically actuated ball valve. Isolating all tunnel vibrations from the two parallel optical tables. Since all parts are independent of one another, accessing any sub assembly is both fast and efficient. The final tunnel in an indraft configuration can be seen in Figure 2.17. This can be changed by inserting a groove lock to tunnel adapter and flexible pipe to pressurize the system.

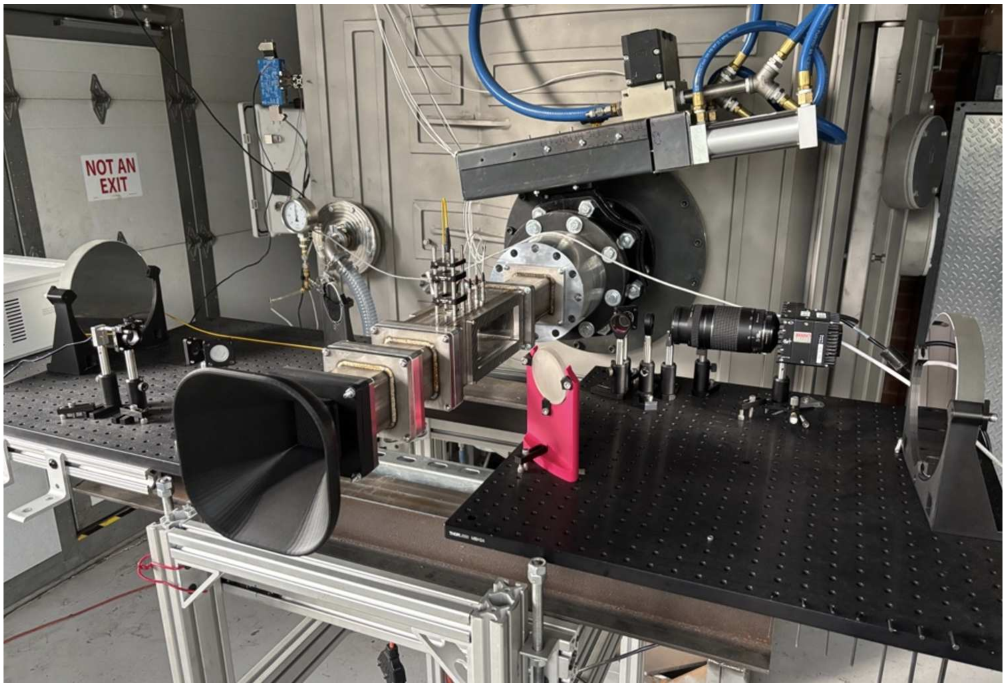

Figure 2.17: Final tunnel configuration with laser ignition system and schlieren

2.7 Control System Design

2.7.1 National Instruments DAQ Hardware

The previous APDL control system used for the supersonic indraft facility utilized Arduino hardware and command line based control over the tunnel. While this was a cost effective and simple system to incorporate, this solution does not facilitate reliable future improvements easily. The initial Arduino setup is shown in Figure 2.18, along with breadboard, control wires, and pressure transducer signal conditioner. In order to update this system it was disassembled, documented, and rebuilt with a more robust NI/LabVIEW system.

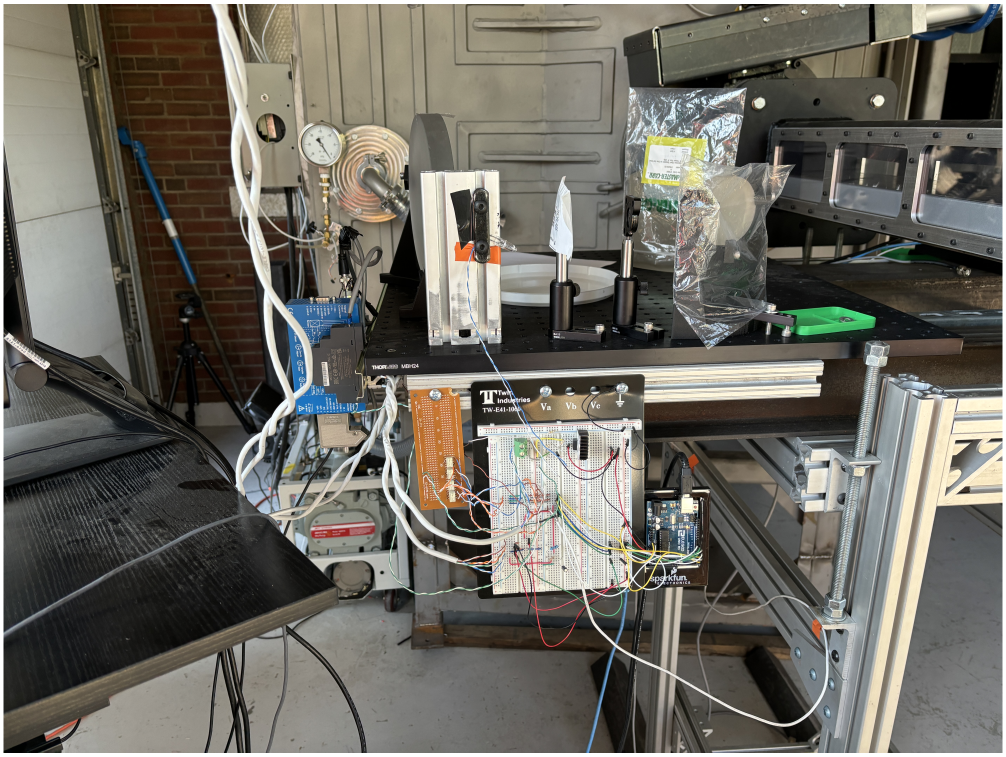

Figure 2.18: Previous APDL Tunnel Control System

A noteworthy aspect of the redesign of the tunnel control system was the need to be isolated from any internet contact. This was done to comply with export control practices and secure handling of APDL data. A National Instruments (NI) 9201 DAQ chassis was chosen to facilitate this role. The control system communicates with our isolated lab computer through standard USB-A cabling. This DAQ body accepts a maximum of four interchangeable NI cards. The technical specifications for these cards and DAQ chassis are detailed in Table 2.1. As we have four dynamic pressure transducers that are sensitive to external EM interference NI 9205 was dedicated to handle these signals. All other pressure transducer measurements are recorded via NI 9234. Control signaling of tunnel functions utilize NI 9472 digital output (DO) card located in slot 3.

Table 2.1: National Instruments DAQ Hardware Information

DAQ Component	DAQ Function	Signal Info	Number of Channels
NI 9201	DAQ Body	NA	4
NI 9205	AI Card	±10 V	32
NI 9234	AI Card	±5 V	4
NI 9472	DO Card	32 VDC	8

A nVent Hoffman electrical housing box that measures 30 inches by 24 inches is mounted to the vacuum chamber for ease of access and reduction of inherent vibrations. This electrical box is fitted with DIN rails for easy mounting of components. In addition, slotted wire ducts separate all major sections of the electrical box. A picture of this system can be seen in Figure 2.19. The NI 9201 system along with cards are aligned at the top right corner of the box furthest from the three-phase 220 V vacuum pump solid state relay.

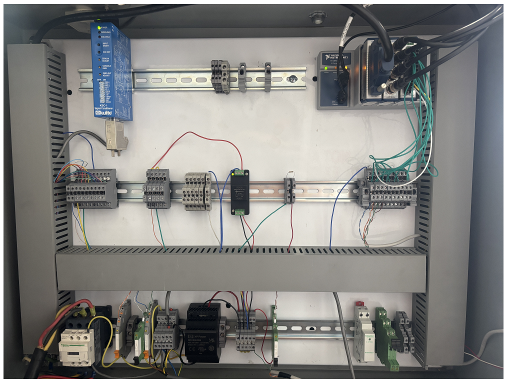

Figure 2.19: Picture of electrical system

The general wiring architecture is shown in Figure 2.20, which provides a systematic overview of the electrical power distribution within the control box. To accommodate the multiple voltage requirements of the facility, (220V, 120V, 24V, and 5V) the wiring is organized into dedicated voltage buses. This modular bus structure simplifies future modifications and enables subsequent users to integrate additional experimental hardware without extensive rewiring or reconfiguration of the primary electrical system.

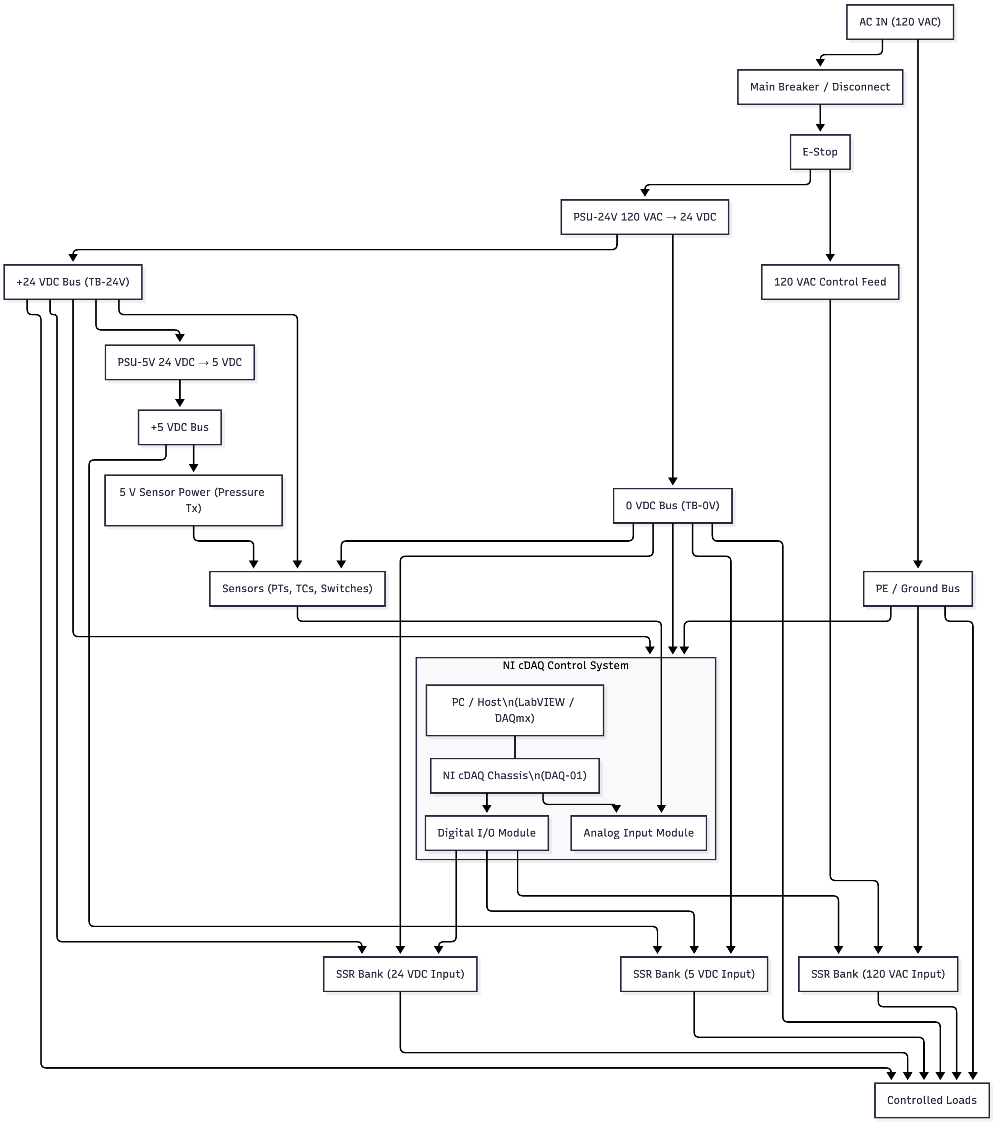

Figure 2.20: Electrical systematic flow chart

2.7.2 LabVIEW

Laboratory Virtual Instrument Engineering Workbench (LabVIEW) is a graphical programming environment widely used for data acquisition, system control, and real-time monitoring in experimental research. The LabVIEW control system developed for this facility was designed from

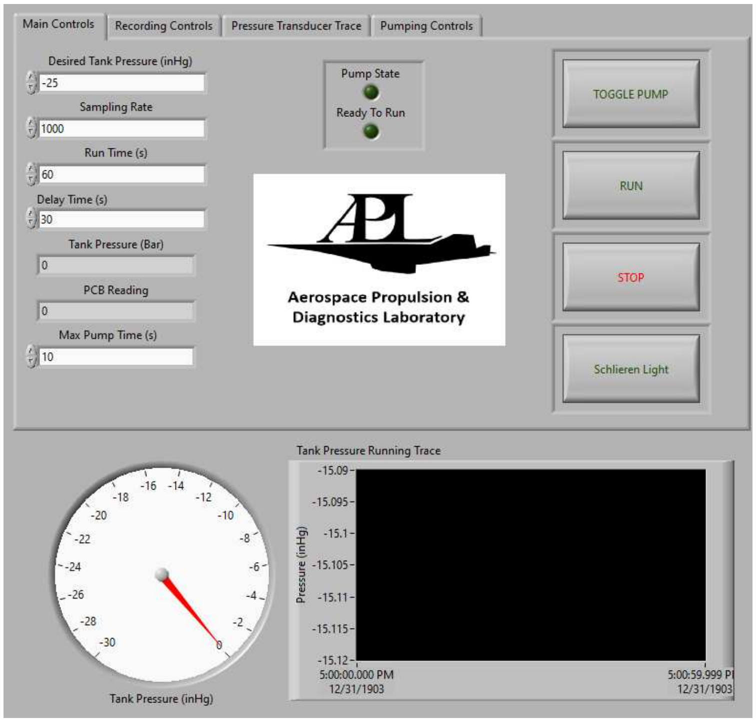

Desired Tank Pressure (inHg): -25
Sampling Rate: 1000
Run Time (s): 60
Delay Time (s): 30
Tank Pressure (Bar): 0
PCB Reading: 0
Max Pump Time (s): 10

Figure 2.21: LabVIEW GUI interface

the ground up to maximize data acquisition rates and minimize computational overhead during high-speed testing. To achieve this, the software architecture separates the test execution sequence from data logging and storage operations, reducing cycle times and preventing buffer overflows that could compromise data integrity. The main GUI control page is presented in Figure 2.21.

The facility control system represents a comprehensive redesign of the previous command line based control, incorporating updated safety protocols, and improved cable management. The modular architecture provides a robust foundation for future experimental development, allowing subsequent users in the APDL to integrate new sensors, actuators, or control logic with minimal modification to the core infrastructure. By leveraging industry-standard National Instruments hardware and the LabVIEW software ecosystem, the system offers both accessibility for routine operation by students and researchers with varying programming experience, and flexibility for advanced users requiring custom modifications or expanded functionality. This balance between ease of use and extensibility ensures the facility remains adaptable to evolving research objectives while maintaining reliable, repeatable operation.

Chapter 3

Experimental Results

3.1 Cold Flow Testing Indraft

Experimental testing in the cold flow configuration focused on validating the inlet Mach number obtained from Equation 2.4. The tests were performed using the configuration shown in Figure 2.17, without igniting the fuel grain. Briefly, the wind tunnel was pumped down to 5 mbar and the test by activating the pneumatic actuator, opening the ball valve that separates the vacuum tank from the test section assembly. Throughout the cold testing campaign both pressure transducer data and high-speed schlieren images were collected. To characterize the flow within the test section, the Kulite XTL-150 static pressure transducer was used. This transducer mounted flush to the top surface of the tunnel measured two distinct aspects of the system pressure. First, the stagnation pressure of the system was measured prior to test operation. Once test flow was introduced, the transducer measured the static pressure within the tunnel for the duration of the test. The actual inlet Mach number was determined experimentally from the Kulite static pressure transducer using the isentropic pressure ratio equation. With some rearrangement Mach number can be solved for using Equation 3.1.

$$\frac{P_0}{P} = \left(1 + \frac{\gamma - 1}{2} M^2\right)^{\frac{\gamma}{\gamma-1}} \rightarrow M_a = \sqrt{\frac{2}{\gamma - 1}\left(\left(\frac{P}{P_0}\right)^{-\frac{\gamma}{\gamma-1}} - 1\right)} \tag{3.1}$$

Shown in Figure 3.1 is the pressure trace collected by the static pressure transducer and the Mach number computed using Equation 3.1. Figure 3.1 left shows that, once the ball valve opens the static pressure at the tunnel wall sharply decreases. As the fluid accelerates through the nozzle, static pressure is converted into dynamic pressure. A stable low-pressure/high-speed flow develops within the test section for 3 seconds, representing the steady-state operational time of the APDL-SFRJ facility. After that, the pressure begins to recover as the vacuum tank has reached a stagnation pressure which unchokes the nozzle downstream of the test section and the fluid decelerates. In Figure 3.1 right, the pressure data is converted into Mach number. The steady-state inlet Mach number was found to be Ma = 0.564, slightly higher than the Ma = 0.5 which was used in the initial design calculations. As the tunnel's initial design assumed mass addition from a burning fuel grain, running the tunnel in a cold flow case would slightly overestimate the inlet Mach number. This indicates that the measured mach number is accurate for both cold and hot flow testing cases.

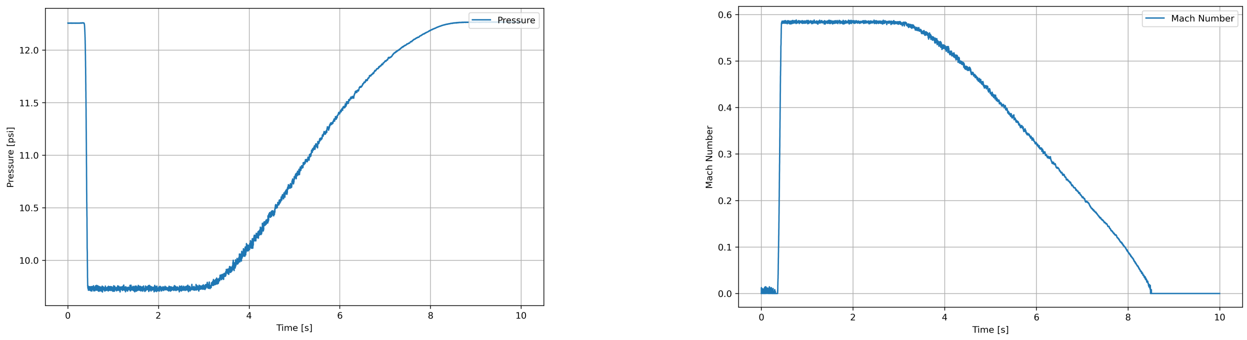

Figure 3.1: Cold Flow Characterization Pressure Trace (left) and Mach number (right)

Along with the pressure transducer data, schlieren frames were recorded to visualize the boundary layer separation off of the backward facing step in a cold flow configuration. A frame from this test can be found in Figure 3.2. In this frame the flow of the tunnel runs from the right side of the frame to the left. The black square in the bottom right corner is the backward facing step geometry. The schlieren setup used a horizontally positioned knife edge at the collector side point source, showing vertical density gradients within the flowfield. As there is no heat release for the duration of this test it can be expected that very few density gradients exist at these subsonic speeds. Knowing this it becomes apparent even at subsonic speeds that flow over the backward facing step dramatically separates the boundary layer and leads to a large velocity gradient.

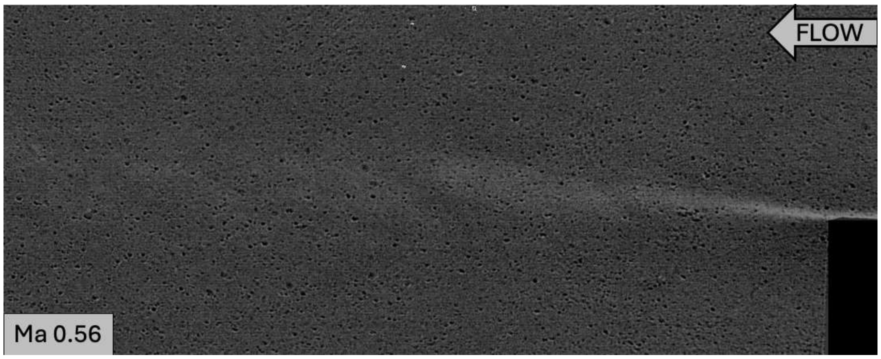

Figure 3.2: Boundary Layer Separation around the backwards-facing step

3.2 Hot Flow Testing Indraft

Hot flow testing under the indraft configuration was performed with the use of the laser ignition system mentioned in Section 2.3.5. An initial ignition location of 0.5 inches from the backward facing step was chosen based on dimensional constraints for the pressure transducer sled. laser ignition was preformed in four configurations. A top down view of the fuel grain is presented in Figure 3.3. A secondary ignition location was later tested where the central beam path was moved downstream by one inch. It is important no note that during all indraft testing, a fuel grain without oxidizer was used. Five variations of this fuel grain were tested with similar results. All of the same benchmark tests were preformed on the last three fuel grain samples. The last of which showed increased reactivity compared to the rest. Hence, the results shown in the following subsections will show results from fuel grain group five.

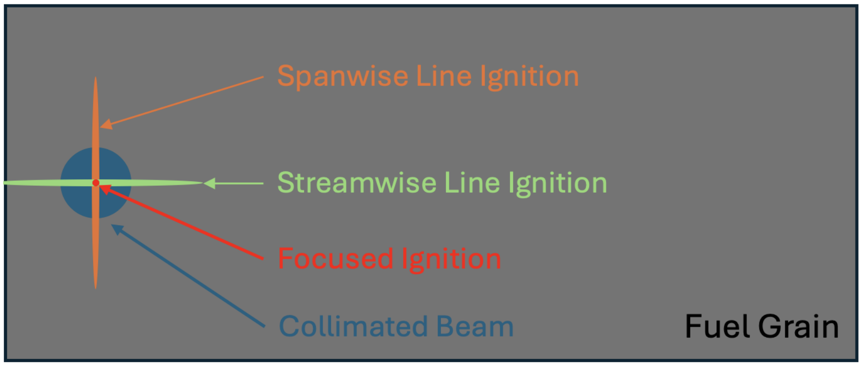

Figure 3.3: Representation of laser ignition surface patters

3.2.1 Initial Laser Ignition Location

Removal of windows on flameholding

Initial testing was conducted with the focused ignition setup where the collimating and focusing lenses were used. Results showed a laser sustained ignition spot on the fuel grain surface. However, the kernel was ultimately extinguished under the full mach 0.56 flow condition. The windows of the test chamber were removed and the same test was conducted to test a configuration with a reduced mach number and an increased streamwise vorticity at the ignition location. This successfully maintained a flame for the 3 second test duration. Figure 3.4-top shows a still frame of the test section where the removal of the test section windows allows for a small localized flame anchored behind the backward facing step during tunnel operation. The cavity stabilizes the flame by generating a strong recirculation zone that can enhance mixing between the free-stream air and the pyrolyzed fuel. Interestingly, the increase in temperature caused by the localized heat release leads to a downward dip of the shear layer, compared with the nonreactive case presented in Figure 3.2. In this configuration the shear layer re-attachment point oscillates during combustion, but the anchoring seems to be on average about 2 cavity heights away from the step. The shear layer attachment point splits the reaction zone into two regions: within the main recirculation zone, we have a heavy soot-laden region where strong light emission is also observed; downstream of the attachment point a diffusion flame is anchored to the surface of the grain. It is important to note that this image was taken while testing the tunnel with the windows removed, as HTPB/MDI is not energetic enough to allow efficient flame anchoring under standard atmospheric conditions using the cavity geometry and inlet Mach number tested herein.

Another important note is that the quality of the schlieren photography drastically changes when the windows are mounted to the test section. As seen in Figure 3.4-bottom the background of the schlieren image becomes grainy and the sensitivity is drastically reduced. This is mainly due to the poor quality of the UV-fused silica windows used in the tests. For future testing, switching to sapphire crystal windows is strongly recommended. Finally, with the windows mounted the heat release region was strictly limited around the laser ignition point which indicates that the effect of side-wall mass addition and generation of streamwise vorticity all play an important role in flame establishment behind a backwards-facing step geometry. The side wall mass addition significantly reduces the mach number in the test section thereby increasing the residence time for the fuel-air mixture to react behind the backwards-facing cavity. In contrast, streamwise vorticity tends to add spanwise coherence around the ignition source resulting in a more distributed ignition source and higher chances for succesful anchoring. To better distinguish between these effects the next set of experiments focused on testing various inlet mach number configurations and different distribution profiles of the ignition source.

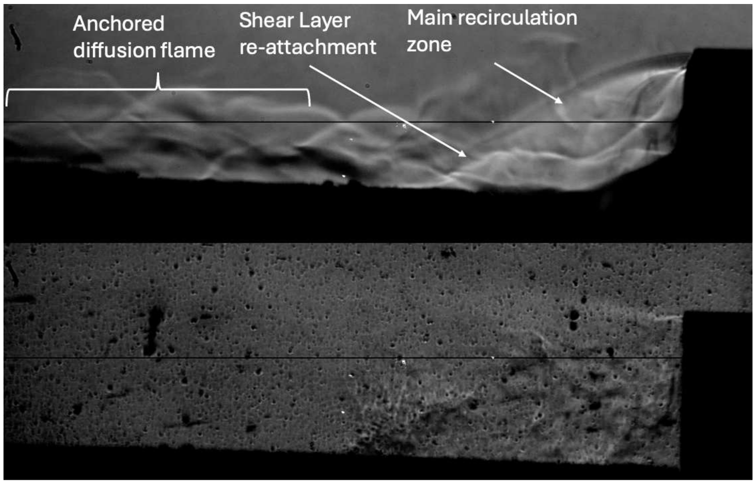

Figure 3.4: Repeated Test Conditions Windows Off (top) and windows on (bottom)

Effect of Test Section Mach Number on Flameholding

To test the effect of inlet Mach number on flame holding, three new choking nozzles were manufactured targeting Ma = 0.26, Ma = 0.16, and Ma = 0.08. Still frames of these mach numbers can be found in Figure 3.5. Interestingly, a reduction in inlet mach number leads to a decrease of the reaction zone behind the step. As the mean flow velocity within the test section decreases, the amount of vorticity caused by the sudden expansion behind the cavity also drops. This leads to less mixing behind the step and forces a much longer shear layer anchoring distance, both having a negative effect on flame development and anchoring. As the Mach number increases the amount of mixing in the recirculation increases. In all three of these cases the flame is immediately extinguished when test section flow begins thus suggesting that inlet Mach number alone is not responsible for the behavior observed in Figure 3.4. Heat release is sustained for the duration of the test through the additional energy addition from the laser ignition system. This continuous source of energy is enough to show up in the schlieren videos.

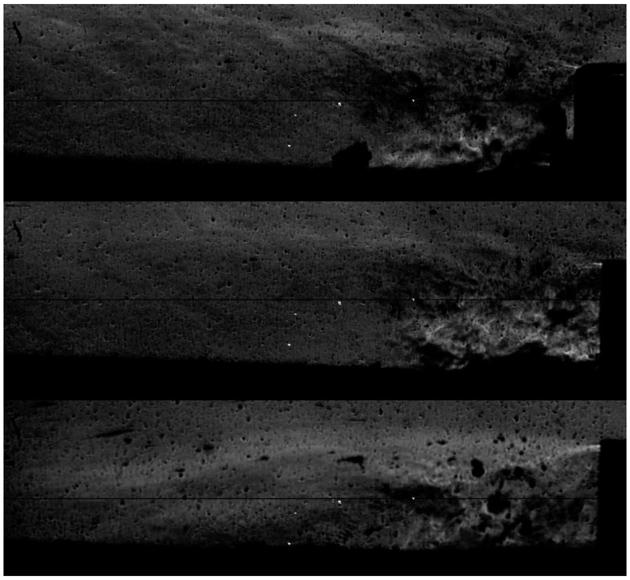

Figure 3.5: Still frames for Mach 0.16 (top), 0.26 (middle), and 0.56 (bottom)

Effect of Laser Ignition Shape on Ignition

Once testing of reduced test section Mach numbers was accomplished, attention shifted to optimizing the coupling of energy between the laser system and the fuel grain surface. In the aforementioned testing both the collimated and focused beam setups consumed all fuel grain in the beam path however the desired spanwise vorticity coherence that led to the early anchroing of the shear layer and consistent heat release behind the backwards facing-step was not achieved. This signified that energy from the laser was not being efficiently utilized past the initial ignition of the grain. To rectify this, the plano-concave cylindrical lens was installed in the laser ignition optical setup to create a one dimensional line ignition source. An example of what this looks like on the fuel grain surface can be found in Figure 3.3. By rotating the cylindrical lens by 90 degrees, the line ignition method was tested in both spanwise and streamwise positions to test effectiveness. Representative frames from this series of testing can be found in Figure 3.6.

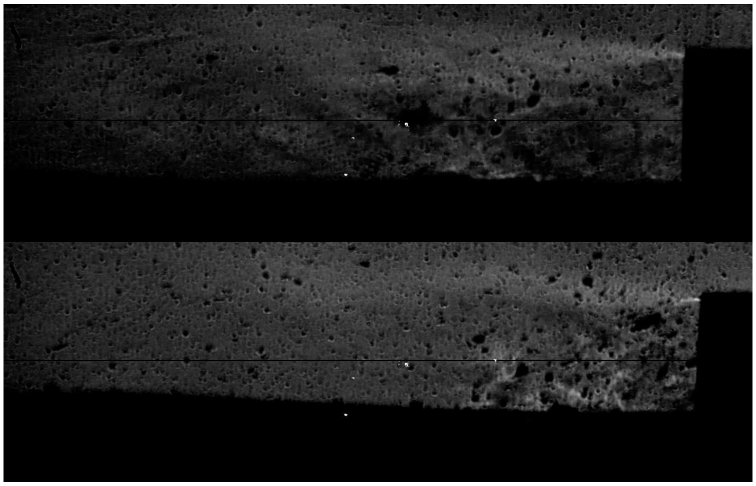

Figure 3.6: Flame structure behind a backwards-facing step using laser line ignition in Spanwise (top) and Streamwise (bottom) configurations

Testing of line ignition showed great promise under ambient conditions; however, the heat release was confined around the ignition zone and did not anchor to the step geometry once the tunnel was turned on. Of the two configurations evaluated, the streamwise ignition setup seemed to performed slightly worse. This is likely due to eddy currents within the backward-facing step region that travel perpendicular to the primary flow direction. The spanwise ignition configuration performed slightly better; however, additional optical losses reduced the energy coupled to the fuel grain surface. Based on these observations, the collimated ignition configuration was determined to be the most effective and was therefore used for the remainder of the testing.

3.2.2 Modified Ignition Location

In addition to the ignition kernel geometry, the optimal location of the energy deposition source was also explored. Placing the ignition location closer to the backward-facing step was expected to improve coupling of the released heat to the surrounding fuel grain because this would ensure continuous mixing between the pyrolized fuel vapors and the incoming air (which gets trapped right at the foot of the step). However, multiple tests demonstrated persistent difficulty in sustaining an active flame on the fuel surface, prompting relocation of the ignition point downstream. Previous test cases indicated that the recirculation zone extended approximately three inches downstream of the backward-facing step. Based on this behavior, the ignition location was moved toward the shear-layer reattachment region on the fuel grain surface, where the circulating flow was expected to advect the flame upstream toward the backward-facing step. Accordingly, a secondary ignition location positioned 1.5 inches downstream of the backward-facing step was selected for evaluation.

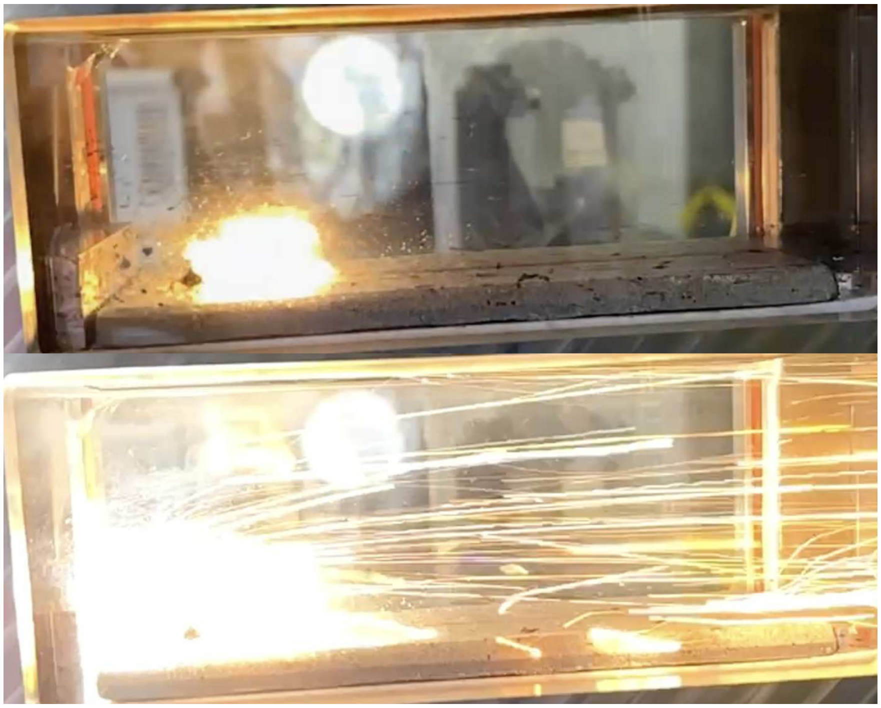

Figure 3.7: Laser Stabilized Flame (Top) and Flair up Event (Bottom)

Testing at the revised ignition location repeated the previously described test matrix, incorporating each ignition geometry and Mach number. These tests confirmed the effectiveness of the collimated beam ignition configuration. With the collimated beam positioned at the adjusted location, stable flameholding was achieved when the laser energy is continuously supplied to the grain throught the entire test. A picture of the igniting kernel can be seen in Figure 3.7-top. Multiple flare-up events were observed, during which large, transient heat-release events were captured on video. These transient phenomena were charactrerized by the appearence of igniting sparks that propagate along the entire length of the test section and the sporadic appearence of a bright combustion zone anchored close the the step surface (see Figure 3.7-bottom). Relocating the ignition point substantially improved flameholding capability. Post-test imaging of the fuel grain indicated localized melting of approximately 0.5 mm of material surrounding the ignition region; however, the flame did not propagate across the fuel grain surface which indicated that the grain reactivity is still too low for the testing conditions available in the tunnel.

Effect of Nitrocellulose lacquer on Ignition

To promote more uniform flame distribution across the fuel grain surface, increased surface reactivity was required. A common method for enhancing initial ignition in solid fuel grains is the application of a thin nitrocellulose lacquer coating. Upon ignition, this surface layer burns rapidly, releasing heat that is coupled into the underlying fuel grain and thereby increasing overall reactivity. Testing of nitrocellulose-coated fuel grains produced a more distributed flame prior to the introduction of test-section flow. However, consistent with previous configurations, the flame was not sustained for the full duration of the test and the flame images looked very similar to what is reported in Figure 3.7.

3.3 Cold Flow Testing Blowdown

Given the limitations encountered both in terms of fuel grain reactivity and wind tunnel stagnation conditions, the SFRJ facility was convered from an indraft (p0=0.85 atm, T0=300 K) to a blowdown facility.

With the addition of the blowdown system, the test platform was no longer constrained by the approximately 3-second test duration imposed by the vacuum chamber. This modification enabled test durations of up to five minutes, with the achievable runtime dictated by the choking nozzle mass flow rate and the desired test pressure. While the system is capable of operating at pressures up to 150 psia, the maximum operating pressure was conservatively limited to maintain the structural integrity of the fused silica optical windows.

To characterize the flow within the test chamber, the system was preset to 10 and 20 psig. At each pressure level, cold-flow pressure traces were recorded. The resulting calibration pressure histories are shown in Figure 3.8.

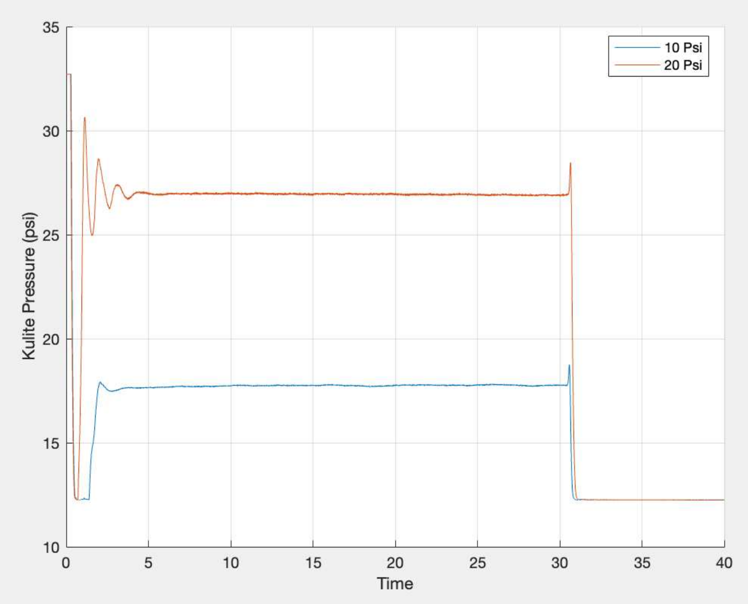

Figure 3.8: Calibration curves for 10 and 20 Psi gauge set pressure

Due to the balanced pressure-reducing regulator located upstream of the test section, a transient startup period was observed as the internal springs equilibrated prior to steady-state operation. The duration of this transient increased with operating pressure. In the indraft configuration, the startup transient lasted approximately 0.5 s, whereas in the high-pressure blowdown configuration it increased to approximately 5 s. This behavior is critical for ignition timing, as initiating fuel grain ignition during the transient startup phase could produce unintended effects on flame development and propagation.

3.4 Hot Flow Testing Blowdown

Hot-flow testing at elevated pressures was conducted using the previously established ignition configuration. Although a sustained flame was observed on the fuel grain surface, no self-sustained flame propagation occurred on the un-oxidized fuel grain. Despite the cumulative improvements to ignition and flameholding, these results indicated that further enhancement was required. Two primary mechanisms for improving flameholding were identified: the introduction of a higher-enthalpy gas heating source and increased fuel grain reactivity. Because commissioning a high-enthalpy source to heat up the gas significantly before the test section would have required substantial additional time and cost, increasing fuel reactivity was selected as the preferred approach for this thesis.

Fuel grain reactivity was enhanced by adding energetic rocket motor material within the HTPB polymeric binder and leveraging the potassium nitrate (KNO_3) content of the propellant. In addition to potassium nitrate, the motor material also contained pure carbon and sulfur. An overview of the fuel grain compositions investigated in this study is provided in Table 3.1. An MDI curative was used to speed up the process.

Table 3.1: KNO_3 laden fuel grain data (weight percents)

Grain Number	HTPB	MDI	KNO_3	Carbon	Sulfur
1	80.475%	12.025%	6.0%	1.125%	0.375%
2	73.95%	11.05%	12.0%	2.25%	0.75%
3	64.38%	9.62%	20.8%	3.9%	1.3%
4	50.46%	7.54%	33.6%	6.3%	2.1%
5	31.32%	4.86%	51.2%	9.6%	3.2%

3.4.1 Revised Ignition Methods

Continuous-wave (CW) laser ignition tests produced localized ignition but no cavity-anchored flame or measurable grain regression. The facility was therefore upgraded to blowdown operation and the grain formulation was doped with crushed KNO_3 propellant to increase ignitability. Following these upgrades, the laser ignition system became unavailable due to hardware damage, prompting the assessment of alternative ignition methods.

Estes Motor Torch

At this stage of testing, the continuous-wave (CW) laser used for remote ignition of the fuel grains became unavailable due to required repairs. As a result, an alternative ignition method was required. This motor ignition system was integrated into the pressure transducer sleds and employed commercially available Estes-class rocket motors to initiate ignition of the fuel grain surface using the exhaust plume and incandescent particles produced during motor operation.

The motor-based ignition method was evaluated under Mach 0.56 flow conditions. During the 0.6 sec burn duration of the starter motor, exhaust sparks were observed impacting the fuel grain surface. Although the heat release associated with the motor was substantial near the motor exit at the top of the test section, a significant portion of this energy was dissipated into the mainstream flow before reaching the fuel grain surface. Figure 3.9 shows a representative frame from this motor ignition event. Following the motor burn, no ignition or sustained interaction with the fuel grain was observed for the remainder of the test.

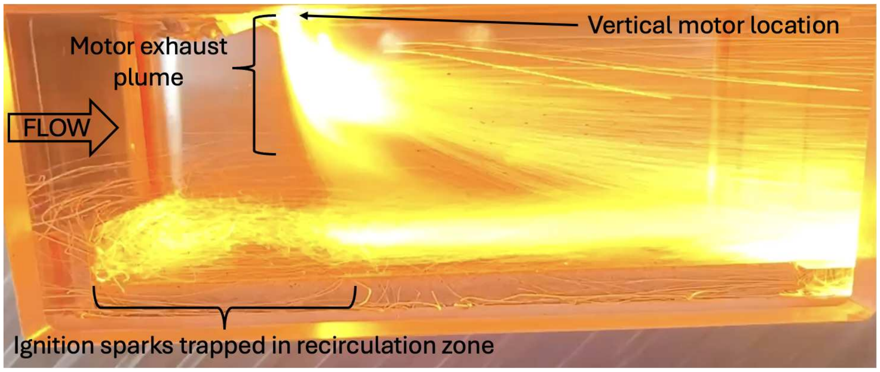

Figure 3.9: Test ignition with Estes motor igniter

Sparks generated within the primary recirculation zone effectively traced both the extent of the recirculation region and the reattachment location of the shear layer on the fuel grain surface. Although this ignition method did not successfully ignite the fuel grain, the incandescent particles seeded throughout the test section provided enhanced visualization of the recirculation zone structure and global flow patterns. Concurrent with flow visualization, pressure traces were acquired to monitor combustion chamber dynamics. A representative pressure trace is presented in Figure **??**, clearly capturing distinct events including the sustained burn phase of the Estes motor and the abrupt pressure spike associated with the motor ejection charge. These pressure signatures confirm

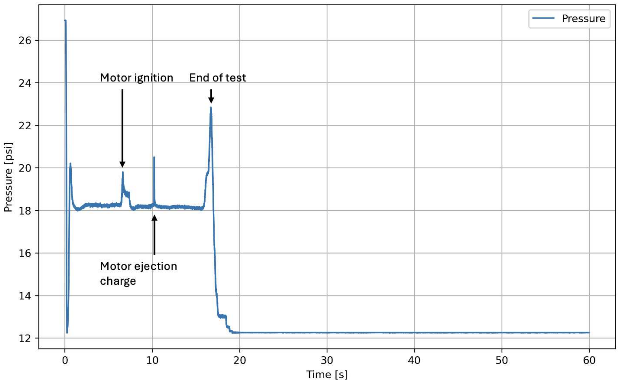

Figure 3.10: Recorded pressure trace with Estes motor igniter

the expected sequence of events and validate the diagnostic capability of the pressure measurement system.

Nichrome Wire Ignition

To more effectively couple energy directly into the fuel grain, a third ignition method was designed and implemented. This approach involved embedding Nichrome heating wire directly into the fuel grain. When connected to a power source, resistive heating from the wire initiated ignition of the surrounding condensed phase, thereby jump-starting the ignition process. This ignition method was applied to all five oxidized fuel grains and was evaluated using both the 0.5-inch and 3-inch cavity configurations. The 3-inch cavity consistently produced improved results relative to the 0.5-inch configuration.

No ignition was observed for fuel grains 1–3. Fuel grain 4 exhibited sustained smoldering for the duration of the test. With a further increase in oxidizer loading in fuel grain 5, a fully sustained flame was achieved for the entire test duration. In this case, the flame was observed to propagate and regress across the fuel grain surface. Representative images of a self sustained flame can be found in Figure 3.11.

Figure 3.11: Regression of fuel grain using grain group five inside of a three inch cavity

Figure 3.12 presents the time histories of the four PCB dynamic pressure transducers for this test. All channels exhibit a strong initial transient period within the first few seconds of operation, characterized by a sharp negative excursion followed by a rapid recovery. This response is attributed to the startup sequence of the facility, during which the flow field and pressure environment undergo rapid adjustment as the tunnel is brought to operating conditions. Following this initial transient, the signals rise to a quasi-steady level between approximately 5 and 12 s, indicating the establishment of a stable flow regime. Minor offsets between the individual transducers are observed during this period, which are consistent with spatial pressure gradients and sensor-to-sensor calibration differences.

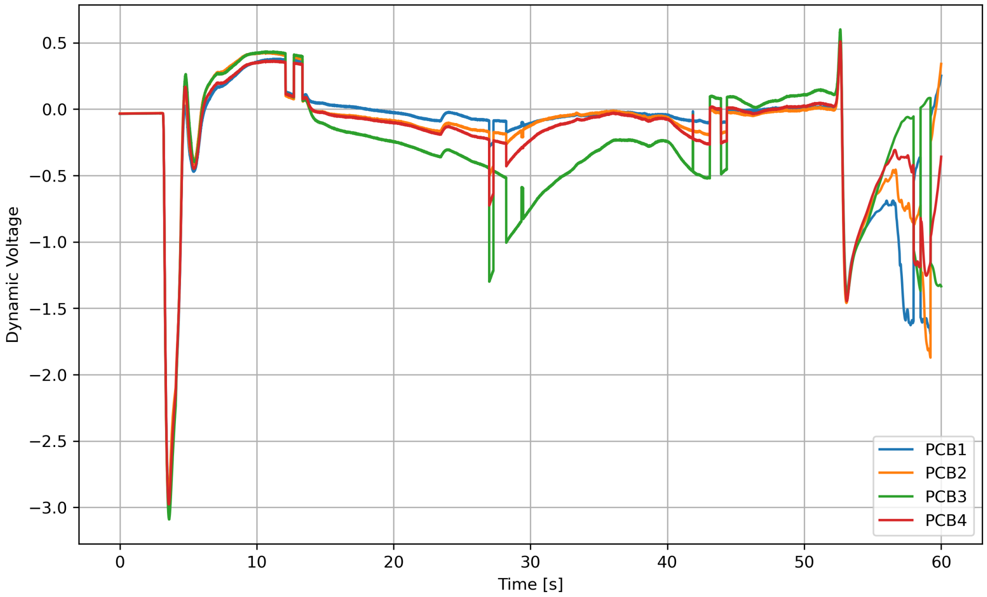

Figure 3.12: Data of PCB dynamic pressure transducers

After the quasi-steady interval, the PCB signals exhibit a gradual drift toward lower differential voltages, indicating a slow reduction in dynamic pressure associated with facility pressure decay and evolving flow conditions within the test section. Several sharp, short-duration excursions are observed throughout the record, most notably near 27s and again near 53s, corresponding to rapid pressure disturbances in the flow. High-speed video acquired during the experiment shows that at approximately 27s a portion of the fuel grain detaches from the fuel grain tray and is evacuated through the tunnel, producing a pronounced transient in all four pressure transducers. At approximately 53 s, the high-pressure supply air valve is closed, causing a sudden loss of flow and termination of tunnel operation. The final portion of the record is characterized by a sharp decrease in all PCB signals, consistent with tunnel shutdown and flow collapse. The close temporal correlation among the four PCB traces indicates that the dominant signal features arise from global flow phenomena rather than localized sensor artifacts, while variations in amplitude reflect differences in sensor placement and sensitivity.

3.4.2 Fuel Grain Regression Analysis

With the improved heat release of the latest fuel grain, fuel grain regression rate calculations could be completed. This was done visually with the use of the video frames taken. The fuel grain regression was calculated using a two step method where a binary mask is applied to the image detecting where the flame front lies. This binary mask then detects the bottom chain of the flame to detect the grain boundary. This step is shown in Figure 3.13 where an example frame is analyzed and the extracted grain profile can be seen. This process is repeated for frames throughout the test, calculating and storing the position of the flame front.

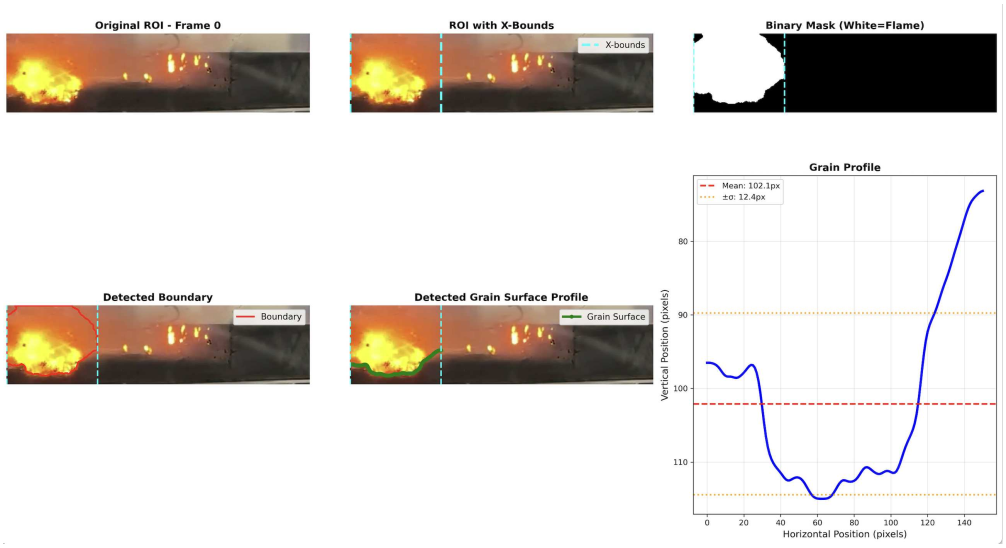

Figure 3.13: Edge detection of flame front

The total regression rate can be calculated by treating the burn area as an expanding semicircle. The distance between points on the grain boundary and an idealized ignition location are stored as an expanding radius. As the real flame front is not a perfect circle there are some variations in the calculated regression rate. These are then averaged to obtain an overall average regression rate for both each frame pair and all of the whole test. An image of this evaluation can be seen in Figure 3.14.

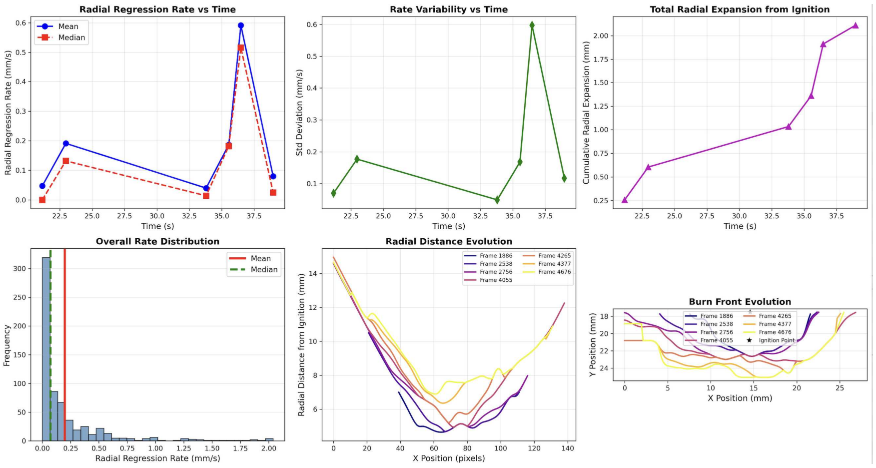

Figure 3.14: Regression rate calculations

Regression rates were calculated using this method using grain group five. The overall average regression calculated through six frame pairs encompassing the test was calculated to be 0.189 mm/sec. While this regression rate may seem low compared to typical burning rates seen in literature. The fuel grain was not an optimized formulation and included a relatively low weight percent of oxidizer. In addition to this, relevant temperatures and pressures of the system were comparatively low when looking at similar facilities outlined in 1.1.

Chapter 4

Conclusions & Future Work

4.1 Summary

A wind tunnel platform was developed at Colorado State University's Aerospace Propulsion and Diagnostics Laboratory to enable controlled experimental investigation of solid fuel ramjet combustion. This manuscript detailed the complete design, manufacturing, integration, and characterization of the wind tunnel as an upgrade to the existing indraft supersonic facility. In parallel, a new high-pressure blowdown system was designed and fabricated, significantly expanding the operational envelope of the APDL by enabling repeatable, long-duration testing at elevated stagnation pressures and mass flow rates. The control system of the facility was rebuilt from the ground up using industry standard NI and LabVIEW to facilitate greater control over tunnel operation and data recording. The facility was outfitted with a high-speed schlieren diagnostic system, providing optical access to the flowfield downstream of a backward-facing step geometry and enabling detailed visualization of shear layer separation, shear layer reattachment, and combustion-induced density gradients. Beyond the baseline backward-facing step configuration, an adjustable-length cavity flameholder was designed and implemented to increase flame blow off limits within the combustor. This modular cavity system allows for systematic variation of geometric parameters while maintaining consistent upstream flow conditions.

Experimental testing demonstrated sustained flameholding at reduced Mach numbers using oxidizer-rich solid fuel grains, confirming the effectiveness of the cavity-based flameholding approach and validating the overall facility design. Collectively, the results establish the wind tunnel as a flexible and well-instrumented platform for fundamental SFRJ combustion studies and provide a foundation for future investigations into fuel formulation, flame stabilization mechanisms, and high-speed combustion dynamics.

4.2 Future Work

Several targeted improvements to the experimental platform would significantly enhance the accuracy, repeatability, and scope of future investigations. The addition of a high-enthalpy air heating system upstream of the test section would increase the reactivity of the incoming flow, enabling ignition and sustained combustion of less reactive solid fuel formulations, including those presented in the indraft testing section of this manuscript. Incorporating controlled preheating would also allow the APDL wind tunnel to more closely simulate a wide range of flight-relevant stagnation conditions, particularly those representative of high-altitude, high-Mach-number operation.

Further improvements could be achieved through testing of professionally manufactured, oxidizer-rich, cleaner-burning solid fuels. These fuels would reduce particulate matter in the exhaust plume, improving schlieren image clarity and overall optical access to the combustion region. In addition to enhancing diagnostic effectiveness, the use of standardized fuel formulations would improve experimental repeatability and enable systematic investigations of combustion stability, flame dynamics, and regression behavior. Continued testing of such fuels would allow for greater validation with results from other test facilities.

Upgrading the current UV-fused silica optical windows to sapphire crystal windows would further improve imaging quality while increasing the allowable operating pressure range of the facility. The improved optical and mechanical robustness of sapphire would support the implementation of advanced diagnostic techniques, including particle image velocimetry (PIV), OH chemiluminescence imaging, and optical flow methods such as the Horn–Schunck algorithm. Together, these diagnostics would enable detailed, time-resolved characterization of velocity fields, reaction zones, and unsteady flame behavior within the combustor.

Bibliography

[1] Kashkhan. Image on wikimedia commons, 2009. Accessed: 2025-09-23.

[2] CSD. The Pocket Ramjet Reader. Technical report, Chemical Systems Division, 1978.

[3] S Gallier. Heterogeneous solid propellants: from microstructure to macroscale properties. In *Progress in Propulsion Physics*, volume 2, pages 21–34, Les Ulis, France, oct 2011. EDP Sciences.

[4] Xingyu Ma and Andreas Schröder. Analysis of flapping motion of reattaching shear layer behind a two-dimensional backward-facing step. *Physics of Fluids*, 29(11), nov 2017.

[5] W.A. Xie and G.N. Xi. Geometry effect on flow fluctuation and heat transfer in unsteady forced convection over backward and forward facing steps. *Energy*, 132:49–56, aug 2017.

[6] William C. B. Senior, Rohan M. Gejji, and Carson D. Slabaugh. Flame Dynamics in an Optically Accessible Solid Fuel Ramjet Combustor. *Journal of Propulsion and Power*, 39(5):718–727, sep 2023.

[7] Pope Alan and Goin Kennith. *High-Speed Wind Tunnel Testing*. John Wiley Sons, 1965.

[8] J. Bruce Ralphin Rose, G. R. Jinu, and C. J. Brindha. A numerical optimization of high altitude testing facility for wind tunnel experiments. *Chinese Journal of Aeronautics*, 28(3):636–648, 2015.

[9] Deborah Pelosi-Pinhas and Alon Gany. Bypass-Regulated Solid Fuel Ramjet Combustor in Variable Flight Conditions. *Journal of Propulsion and Power*, 19(1):73–80, jan 2003.

[10] Ronald G. Veraar and Wolter Wieling. Sustained Combustion Limits of a Central Dump Solid Fuel Ramjet Combustor at High Altitude Operational Conditions. In *2018 Joint Propulsion Conference*, pages 1–19, Reston, Virginia, jul 2018. American Institute of Aeronautics and Astronautics.

[11] Adela Ben-Yakar and Ronald K Hanson. Cavity Flame-Holders for Ignition and Flame Stabilization in Scramjets: An Overview. *Journal of Propulsion and Power*, 17(4):869–877, jul 2001.

[12] Ronald S. Fry. A Century of Ramjet Propulsion Technology Evolution. *Journal of Propulsion and Power*, 20(1):27–58, jan 2004.

[13] Amir Aziz, Rizalman Mamat, Wan Khairuddin Wan Ali, and Mohd Rozi Mohd Perang. Review on Typical Ingredients for Ammonium Perchlorate Based Solid Propellant. *Applied Mechanics and Materials*, 773-774(15):470–475, jul 2015.

[14] Vesna Rodić and Mirjana Petrić. The effect of curing agents on solid composite rocket propellant characteristics. *Scientific Technical Review*, 55(1):46–50, 2005.

[15] Uma Vellaisamy and Shelly Biswas. Effect of metal additives on neutralization and characteristics of AP/HTPB solid propellants. *Combustion and Flame*, 221(4):326–337, nov 2020.

[16] ROBERT ZURAWSKI and JAMES GREEN. An evaluation of metallized propellants based on vehicle performance. In *23rd Joint Propulsion Conference*, Reston, Virigina, jun 1987. American Institute of Aeronautics and Astronautics.

[17] Izham Izzat Ismail, Norhuda Hidayah Nordin, Muhammad Hanafi Azami, and Nur Azam Abdullah. Metals and Alloys Additives as Enhancer for Rocket Propulsion: A Review. *Journal of Advanced Research in Fluid Mechanics and Thermal Sciences*, 90(1):1–9, dec 2021.

[18] Lin Chen, Keisuke Asai, Taku Nonomura, Guannan Xi, and Tianshu Liu. A review of Backward-Facing Step (BFS) flow mechanisms, heat transfer and control. *Thermal Science and Engineering Progress*, 6(January):194–216, jun 2018.

[19] Jay V Evans. *CHARACTERIZATION OF THE SECONDARY COMBUSTION ZONE OF A SOLID FUEL RAMJET*. Master of science in aeronautics and astronautics, Purdue University, 2021.

[20] M.T. Boyle. *Low speed wind tunnel testing*. Wiley-Interscience, 3 edition, 1988.

[21] R.D. Mehta and P. Bradshaw. Design rules for small low speed wind tunnels. *The Aeronautical Journal*, 83(827):443–453, nov 1979.

[22] Jack D. Mattingly and Keith M. Boyer. Elements of Propulsion: Gas Turbines and Rockets Second Edition. In *Elements of Propulsion: Gas Turbines and Rockets, Second Edition*, pages i–lxxiv. American Institute of Aeronautics and Astronautics, Inc., Reston, VA, jan 2016.

[23] William H. Heiser and David T. Pratt. *Hypersonic Airbreathing Propulsion*. American Institute of Aeronautics and Astronautics, Reston, VA, 1994.

[24] Stephen R. Turns. An Introduction to Combustion: Concepts and Applications (3rd ed.)., 2012.

[25] J DRISCOLL. Turbulent premixed combustion: Flamelet structure and its effect on turbulent burning velocities. *Progress in Energy and Combustion Science*, 34(1):91–134, feb 2008.

[26] Martin Chiaverini and Kenneth Kuo. *Fundamentals of Hybrid Rocket Combustion and Propulsion*. American Institute of Aeronautics and Astronautics, Reston ,VA, may 2007.

[27] Merrill Beckstead, Vigor Yang, and K. Puduppakkam. Modeling and Simulation of Combustion of Solid Propellant Ingredients Using Detailed Chemical Kinetics. In *40th AIAA/ASME/SAE/ASEE Joint Propulsion Conference and Exhibit*, number July, Reston, Virigina, jul 2004. American Institute of Aeronautics and Astronautics.

[28] John D. Anderson. *Modern Compressible Flow: with historical perspective — Second edition. J.D. Anderson. McGraw-Hill Book Co (UK), McGraw Hill House, Shoppenhangers Road, Maidenhead, Berks, SL6 2QL. 1990. 650 pp. Illustrated. £18.95.* McGraw-Hill Education, Boston, 4 edition, sep 2003.

[29] E.T. Curran and S.N.B. Murthy. *Scramjet Propulsion*. American Institute of Aeronautics and Astronautics, Reston ,VA, jan 2001.

[30] William H. Rae and Alan Pope. *Low-Speed Wind Tunnel Testing*. John Wiley & Sons, New York, NY, 1984. Includes methodology and calibration procedures for low-speed wind tunnel testing.

[31] Aeronautical Society of Great Britain. *Seventh Annual Report of the Aeronautical Society of Great Britain, for the Year 1872*, volume 7 of *Annual Report of the Aeronautical Society of Great Britain*. Henry Richardson for the Aeronautical Society of Great Britain, Greenwich and London, United Kingdom, 1872. Public domain; no DOI found; accessed via digital library.

[32] Philip Stich, Dennis Rose, Nick Smoliga, Kevin Sipe, and Michael Mills. Sustainment program for the 16-ft tunnels in the propulsion wind tunnel facility at the arnold engineering development center. *36th AIAA Aerospace Sciences Meeting and Exhibit*, 1998.

[33] M. L. Mills. Supplemental calibration of the aedc–pwt 6-foot transonic tunnel aerodynamic test section. Technical Report AEDC-TR-80-32, Arnold Engineering Development Center, June 1981.

[34] Michael L. Mills. Feasibility of operating the AEDC Supersonic Wind Tunnel (16S) up to Mach number 6. *AIAA Paper*, (6):7353–7358, 2004.

[35] W. T. Schaefer. Characteristics of major active wind tunnels at the langley research center. Technical Memorandum TM X-1130, NASA Langley Research Center, July 1965.

[36] Jeffrey S. Hodge and Stephen F. Harvin. Test capabilities and recent experiences in the NASA Langley 8-foot high temperature tunnel. *21st Aerodynamic Measurement Technology and Ground Testing Conference*, (June), 2000.

[37] VA S.F. Harvin and K.F. Cabell NASA Langley Research Center Hampton, S.D. Gallimore, VA Swales Aerospace Hampton, and VA G.L. Mekkes Jacobs Sverdrup Hampton. Test Capability Enhancements to the NASA Langley 8-Foot High Temperature Tunnel. *JANNAF 41st*

Combustion/29th Airbreathing Propulsion/23rd Propulsion Systems Hazards Joint Subcommittee Meeting, pages 1–16, 2006.

[38] Mark R. Woike and Brian P. Willis. The nasa glenn research center's hypersonic tunnel facility. In Alan Pope, editor, *Wind Tunnel Testing*, chapter 16. NASA, Washington, DC, 2001.

[39] C. J. Pirrello, R. D. Hardin, M. V. Heckart, and K. R. Brown. An Inventory of Aeronautical Group Research Facilities. Volume 1: Wind Tunnels. *NASA Contractor Report*, 1, 1971.

[40] Jerrod W. Hofferth and Daniel R. Ogg. Reactivation of VKF Wind Tunnel D by AFRL at AEDC: Supersonic Performance and Freestream Characterizations. In *AIAA Aviation 2019 Forum*, number June, Reston, Virginia, jun 2019. American Institute of Aeronautics and Astronautics.

[41] Christopher J. Clifford. *Design and Characterization of a Supersonic Wind Tunnel for the Study of Shock Wave Boundary Layer Interactions*. Master, The Ohio State University, 2010.

[42] Joji Matsumoto. *Design and Testing of a Subscale Supersonic Aeropropulsion Wind Tunnel*. Master, THE UNIVERSITY OF TEXAS AT ARLINGTON, 2000.

[43] Christopher W Larson. *The Design and Construction of a 20" x 20" Mach 2.0 Blowdown Wind Tunnel to Characterize the Lift and Drag of Irregularly Shaped Fragments*. Master, Virginia Polytechnic Institute and State University, 2011.

[44] Jason Solomon. *THE DESIGN, CALIBRATION, AND COMMISSIONING OF A BENCHMARK HYPERSONIC WIND TUNNEL*. Master, University of North Carolina at Charlotte, 2021.

[45] Frank Giardino and Joana Rocha. Design and Characterization of a High-Speed Subsonic Aeroacoustic Wind Tunnel. *Journal of Aircraft*, 56(1):108–120, jan 2019.

[46] Philip Andrews, Philip Lax, Skye Elliott, Alexander Firsov, and Sergey Leonov. Flow Characterization at Heated Air Supersonic Facility SBR-50. *Fluids*, 7(5):168, may 2022.

[47] Scott Best, David Van Every, John A. Strike, and Rajan Kumar. Commissioning of a Polysonic Wind Tunnel at the Florida State University. In *53rd AIAA Aerospace Sciences Meeting*, number January, pages 1–13, Reston, Virginia, jan 2015. American Institute of Aeronautics and Astronautics.

[48] Joshua Gary and Davide Vigano. New testing capabilities of the missouri university of science and technology supersonic wind tunnel. In *AIAA SciTech Forum*, 2024. Documentation of facility upgrades, modular test section design, and advanced diagnostics for the Mach-3 supersonic wind tunnel at Missouri S&T.

[49] Daniel K Johnson. *the Design and Implementation of a Supersonic Indraft Tube Wind Tunnel for the Demonstration of Supersonic Flows*. Master, California Polytechnic State University, 2018.

[50] Spencer Teeter, Katie Plese, Rebecca Zulch, Caleigh Haid, Bret Windom, Azer P. Yalin, and Ciprian Dumitrache. Development of a Supersonic Wind Tunnel Facility for Scramjet Testing at Colorado State University. In *AIAA SCITECH 2024 Forum*, Reston, Virginia, jan 2024. American Institute of Aeronautics and Astronautics.

[51] Edward T. Schairer. Three-Dimensional Adaptive-Wall Wind Tunnel. Technical report, NASA Ames Research Center, 1983.

[52] Jerrod W. Hofferth and Daniel R. Ogg. Reactivation of VKF Wind Tunnel D by AFRL at AEDC: Overview and Subsystem Checkout Results. In *22nd AIAA International Space Planes and Hypersonics Systems and Technologies Conference*, number September, Reston, Virginia, sep 2018. American Institute of Aeronautics and Astronautics.

[53] Rachel Ben-Arosh and Alon Gany. Similarity and scale effects in solid-fuel ramjet combustors. *Journal of Propulsion and Power*, 8(3):615–623, may 1992.

[54] Roni Zvuloni, Alon Gany, and Yeshavahou Levy. Geometric effects on the combustion in solid fuel ramjets. *Journal of Propulsion and Power*, 5(1):32–37, jan 1989.

[55] William C B Senior. *APPLIED LASER DIAGNOSTICS TO INVESTIGATE FLOW-FLAME INTERACTIONS IN A SOLID FUEL RAMJET COMBUSTOR*. Doctor of philosophy, Purdue University, 2023.

[56] Jay V Evans. *EXPERIMENTAL MEASUREMENT AND MODELING OF REGRESSION RATE PHENOMENA IN SOLID FUEL RAMJET COMBUSTORS*. Doctor of philosophy, Purdue University, 2023.

[57] Ryan D. DeBoskey, David A. Kessler, Trushant K. Patel, Brian T. Bojko, Ryan Johnson, Gabriel B. Goodwin, Venkateswaran Narayanaswamy, and Andrew Hess. Analysis of Flame Structures in a Model Solid Fuel Ramjet Combustor with Increasing Reynold's Number. In *AIAA SCITECH 2024 Forum*, Reston, Virginia, jan 2024. American Institute of Aeronautics and Astronautics.

[58] Dominic Gallegos, Henry Pace, Charles Arnold, Luca Massa, and Gregory Young. Regression and Flame Structure in Cavity Flameholding Solid-Fuel Ramjet Fuel Grains. *Journal of Propulsion and Power*, 39(6):800–810, nov 2023.

[59] Youri Prokesch, Abram Duran, Dominic Gallegos, Ethan Schlussel, and Gregory Young. Effect of flameholding cavity geometry on the flowfield of a solid fuel scramjet. *Acta Astronautica*, 224(August):508–519, nov 2024.

[60] Omer Musa, Chen Xiong, and Zhou Changsheng. Combustion characteristics and turbulence modeling of swirling reacting flow in solid fuel ramjet. *Acta Astronautica*, 139:1–17, oct 2017.

[61] G Schulte. Fuel regression and flame stabilization studies of solid-fuel ramjets. *Journal of Propulsion and Power*, 2(4):301–304, jul 1986.

[62] Brian Evans, Nicholas Favorito, and Kenneth Kuo. Study of Solid Fuel Burning-Rate Enhancement Behavior in an X-ray Translucent Hybrid Rocket Motor. In *41st AIAA/ASME/SAE/ASEE Joint Propulsion Conference Exhibit*, Reston, Virigina, jul 2005. American Institute of Aeronautics and Astronautics.

[63] F Schultz-Grunow and K Wieghardt. STUDIES ON WIND TUNNEL STRAIGHTENERS. Technical Report 3, 1942.

Appendix A

Wind Tunnel Operating Steps

Table A.1: Test Information

Test Name	SFRJ Group 4	**Date**	2025-11-03
Prepared By	Riley Duffens	**Location**	Powerhouse - APDL
Supervisor	Ciprian Dumitrache	**Operator**	Riley Duffens
Test ID	Test # 12	**Data File Path**	Hardrive/Tests/ Group4/Test12
LabVIEW VI	WindtunnelVI2.0	**DAQ Mapping**	AI0-AI1 AI0-AI3 DO0-DO6

1. Objective

Operate the SFRJ indraft wind tunnel to test fuel grain combustion. Results from tests include pressure transducer data, and high-speed frame data captured from both iPhone camera and phantom camera.

2. Scope

This procedure is intended for trained students operating the APDL wind tunnel. It covers pre-test checks, setup, data acquisition, shutdown, and documentation.

3. Equipment

Equipment	Description	Notes
Wind Tunnel	Intermittent indraft configuration	Verify all bolts are in place and tight
LabVIEW	DAQ & control interface (NI chassis/modules)	Confirm drivers and VI is open
Pressure Transducers	4 X Kulite XTL-190S-25A, PCB 113B28	Ensure chanels are mapped, Ensure PCB signal conditioner is on
Computer	Lab PC with LabVIEW	Confirm save directory to secure hard drive

4. Safety Precautions

- Verify the emergency stop for run sequence is working
- Confirm all DAQ and transducer wiring is correct before enabling power
- Open windows to vent any potential fumes after test is conducted

5. Test Setup

A) Fuel Grain Setup

☐ Ensure that grain sled is clear of old super glue or left over fuel grain

☐ If dirty clean with ultrasonic cleaner, then with wiping clean

☐ Apply superglue to fuel grain sled top surface in 6 positions distributed along the corners and center

☐ Place fuel grain onto fuel grain sled and hold in place with lab weights

☐ Wait 5 minutes for super glue to bond to fuel grain and grain sled steel

B) Tunnel Assembly

☐ Ensure that grain sled is clear of old super glue or left over fuel grain

☐ If dirty clean with ultrasonic cleaner, then with wiping clean

☐ Apply superglue to fuel grain sled top surface in 6 positions distributed along the corners and center

☐ Place fuel grain onto fuel grain sled and hold in place with lab weights

☐ Wait 5 minutes for super glue to bond to fuel grain and grain sled steel

Tunnel Assembly

☐ Slide fuel grain sled into tunnel, affix fasteners from bottom of tunnel

☐ Place Teflon window spacers at bottom and top of window locations

☐ Insert window and place window retainer plate on outside of tunnel

☐ Fasten at least 4 of the 8 window retaining screws through the window retaining plate and into the tunnel. Hand tighten only

☐ Place pressure transducer sled on top of tunnel and screw CW fiber optic into optic port

☐ Tighten at least 4 of the 6 pressure transducer bolts

☐ Line up flow straightening assembly and fasten assembly onto intake side of test section

☐ Tighten all 4 bolts and nuts holding intake assembly onto test section

C) LabVIEW Setup

☐ Ensure pressure transducers are hooked up correctly and are reading in LabVIEW

☐ Check sampling rate, test time, and ambient pressure reading

☐ Write CSV file name for data saving on second page of LabVIEW

6. Test Procedure Indraft

- ☐ Turn on laser power and laser cooler power, check for leaks in the coolant line connections
- ☐ Ensure LabVIEW is running
- ☐ Turn Laser on and wait for steady flame on fuel grain surface
- ☐ Click RUN on LabVIEW interface
- ☐ Wait for duration of test watching for any test anomalies
- ☐ Move data to the UMT secure drive

Test Shutdown

- ☐ Turn off laser power, and laser cooler power
- ☐ Take flow conditioning section off of test section
- ☐ Remove pressure transducer sled
- ☐ Remove windows, clean soot and particulate matter
- ☐ Remove fuel grain sled and separate old fuel grain from sled
- ☐ Remove optical window from pressure transducer sled and clean
- ☐ Ensure all data is saved and backed up
- ☐ Stop LabVIEW sequence
- ☐ Cleanup workbench and optical tables

7. Data Recording & Notes

Ambient Conditions:

Temperature (C)	Pressure (kPa)	Humidity	Operator	Start Time	End Time

Testing Conditions Log:

Test Duration (s)	Laser Power (w)	Ambient Pressure (kPa)	Tank Pressure	Comments

Test Observations / Issues:

8. Verification & Sign-off

Name / Signature	Role	Date